

Studying the spectral variability of 4U 0115+63

Master's Thesis in Physics

Presented by

Katrin Berger

October 18, 2022

Astronomical Institut Dr. Karl Remeis-Sternwarte

Friedrich-Alexander-Universität Erlangen-Nürnberg

Department Physik



Supervisor: Prof. Dr. Jörn Wilms

Abstract

This thesis focuses on the spectral analysis of the High Mass X-ray binary system 4U 0115+63. Since its discovery, this source has sparked the interest of scientists because of its prominent spectral features. 4U 0115+63 combines the, up to now, highest number of observed cyclotron resonant scattering features, a pronounced quasi-periodic oscillation and a “10 keV feature” in its spectrum. The aim of the analysis performed in this thesis is to get a better understanding of the still sparsely understood “10 keV feature”. This project was already started in the foregoing bachelor’s thesis Berger (2019). Here I begin the analysis by redoing the previous work using additional data and a more detailed approach. Following that, the examination of the observations is continued further, which lead to new results.

I start the analysis by using data from the Nuclear Spectroscopic Telescope Array (*NuSTAR*) and the Neil Gehrels Swift Observatory (*Swift*). I describe the continuum of the spectrum using a power-law with an high energy cut-off. Additionally cyclotron lines and a broad Gaussian feature, to account for the “10 keV feature”, were used. Here this fit was further improved by using four cyclotron lines in total and a more precise description of the iron lines. This resulted in a reduced χ^2 of 1.50 for the earlier taken set of observations and a reduced χ^2 of 1.42 for the later observations. Fitting only the averaged *NuSTAR* data resulted in a reduced χ^2 of 1.49 and 1.53 for the first, respectively second, observation.

Following Berger (2019), partial spectra of the observed peaks and the off-peak states were extracted. The change in the overall shape of the spectrum around ~ 10 keV during these different states of the observation could be verified. This behavior was further examined by using two additional approaches to partition the observed data. This way I could prove that the observed spectral change depends stronger on the relative intensity and not exclusively on the phase of the QPOs.

I continued the analysis by calculating 2 dimensional confidence contours for the parameters of the fundamental cyclotron line, the “10 keV feature” and the flux of the power-law. These confidence contours did not show signs of a correlation between the parameters of the fundamental cyclotron line. However a strong anti-correlation between the flux and the energy of the “10 keV feature” was detected, that is independent of the observed count rate. The second proven anti-correlation was detected between the flux of the “10 keV feature” and the flux of the cut-off power law. Here an additional intensity dependency of the contours could be verified.

In addition to this Master’s thesis, the findings discussed in this work will also be published in a forthcoming paper.

Contents

1	Introduction	7
2	Theoretical background	9
2.1	X-ray binary systems	9
2.1.1	High Mass X-ray Binary (HMXB)	10
2.2	Cyclotron Resonant Scattering Features (CRSFs)	12
2.3	Quasi-periodic oscillations (QPOs)	14
2.4	The 10 keV feature	16
3	4U 0115+63	19
4	Instruments	25
4.1	Wolter-I optics	25
4.2	The Nuclear Spectroscopic Telescope Array (NuSTAR)	26
4.3	The Neil Gehrels Swift Observatory (Swift)	28
5	Observations and data reduction	29
6	Data analysis	31
6.1	Spectral modeling	31
6.1.1	Combined NuSTAR and Swift data	32
6.1.2	Cross-calibration between NuSTAR and Swift	34
6.1.3	NuSTAR data	38
6.2	Hardness-Intensity plots	38
6.3	Flux-resolved spectroscopy	42
6.3.1	Selected Off-peak / Peak states	42
6.3.2	Time-resolved spectroscopy	42
6.3.3	Selected rates	47
6.3.4	2 dimensional confidence contours	58
7	Conclusion and Outlook	61

Chapter 1

Introduction

The unique characteristics of compact stellar objects create extreme conditions in their surroundings that cannot be replicated on earth. Measuring devices on board satellites can provide us with observational data consisting of, e.g., light curves and spectra, of these sources. This information helps us gain knowledge about the stellar objects and their locations. These measurements also enable the possibility of testing theories of physical principles under the conditions prevailing there. In addition, the observations can also lead to discoveries that are not yet described by current theories which can then be used to expand our current understanding. Some sources combine both aspects by containing well understood spectral components in combination with more rare features of yet unknown origin. An example is the source 4U 0115+63, studied in this thesis. It has been observed by numerous detectors in recent decades and is well-studied in terms of its cyclotron lines. However the spectra of this source also contain an additional feature at ~ 10 keV, the so-called “10 keV feature”, that still poses an open question.

This thesis resumes the work done in the Bachelor’s Thesis Berger (2019) to study this “10 keV feature”.

To do so, the previous analyses were redone using the updated calibration software for the extractions and further extended to gain new information about this additional spectral feature of 4U 0115+63.

This thesis begins with a description of the general properties of X-ray binary systems and their most prominent spectral features in chapter 2. 4U 0115+63 is introduced in chapter 3. In chapter 4 the satellites that were used to observe the data analysed in this work, namely *NuSTAR* and *Swift*, are discussed. Chapter 5 focuses on the observations that were used for the analysis and the reduction of these data sets. In chapter 6 the analysis of the observational data is explained. The spectral fit performed and its improvements compared to Berger (2019), to get a more detailed description of the modeled data, are described in section 6.1. Section 6.3 focuses on the partitioning of the observations, using three different approaches, to gain more information about the spectral feature that was described in Berger (2019). Afterwards the correlations between different parameters of the spectral fit are examined in subsection 6.3.4 by analysing 2-dimensional confidence contours. Lastly the results are summarized in chapter 7 and an outlook for further studies is given.

Chapter 2

Theoretical background

In this chapter, information on astronomical systems and some of their spectral features necessary to understand the following analysis, are given.

2.1 X-ray binary systems

Depending on their initial mass, the final stages of a star can vary between a white dwarf (WD), a neutron star (NS) or a black hole (BH). However these stellar objects can exist not only in isolation or in star clusters, but also in systems where two stars are gravitationally bound to each other and orbit around a common center of mass, forming a stellar binary.

If a significant amount of mass is transferred between the two stellar objects, the system is called an X-ray binary. In this case the accretor, usually a compact object, uses its strong gravitational field to accrete mass from its companion, the donor. In the majority of cases the donor is either a young star or a star in the later stages of the main sequence.

The mass transfer onto the accretor releases energy that can further interact with e.g. elementary particles and lead to the generation of X-rays, see also Ballhausen (2021). The accretion mechanism by which this mass transfer takes place depends on the properties of the binary system.

In Figure 2.1, one can see that both objects of the binary system are surrounded by a black envelope that denotes the extent of their gravitational forces. The equipotential point where the gravitational exertion of both parties in the bound system cancels out is known as the first Lagrange point L_1 . The area around the objects that are within the envelope are called their Roche lobes. If the donor star fills up its Roche lobe, matter can flow via L_1 over to the Roche lobe of the accretor. Continuous transfer of matter in this way can form an accretion disc around the compact object, leading to a constant supply of matter onto the accretor (Tauris & van den Heuvel, 2006). A schematic illustration of this so-called Roche lobe overflow is shown in the lower part of Figure 2.1.

Another case that can be seen in the upper plot of Figure 2.1, is the wind accretion. There, the donor does not completely fill its Roche lobe, but has a strong stellar wind that is partially accreted onto the compact object (Tauris & van den Heuvel, 2006).

X-ray binaries can be further categorized based on the type of accretor in the system, and also by the spectral type or mass of the optically visible companion.

Here the typical categories are Low Mass X-ray binaries (LMXB), for donor stars with a mass lower than $1 M_{\odot}$, or High Mass X-ray binaries (HMXB), with masses of more than $10 M_{\odot}$. In

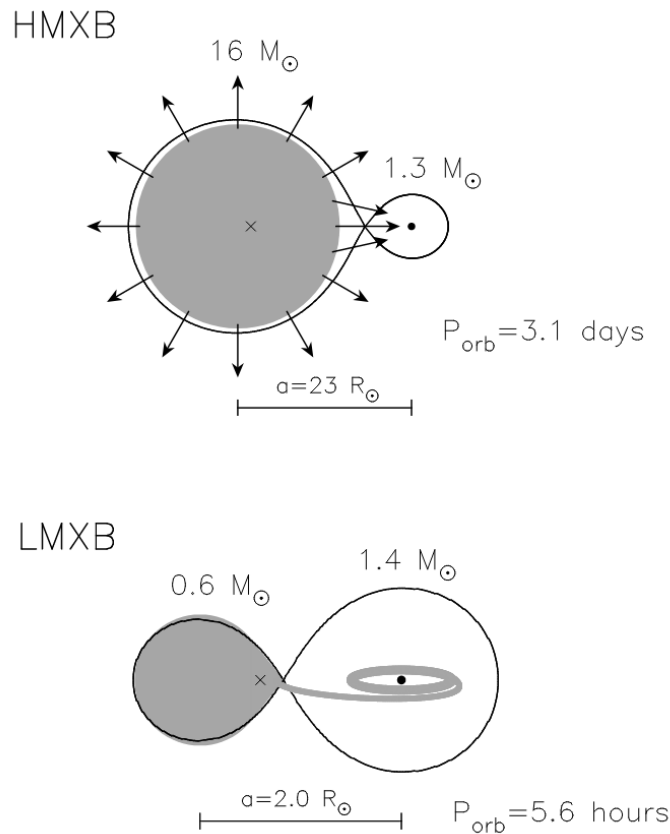


Figure 2.1: Two possible accretion mechanisms of binary systems. The upper plot shows a star with a high mass that emits a strong stellar wind. Part of that stellar wind is accreted onto the compact object. The lower plot shows a less massive star that filled up its Roche-lobe. The matter can then flow over to the compact object and supply its accretion disc. Image taken from Tauris & van den Heuvel (2006).

the rare case that the mass of a donor star lies between these two boundaries, e.g. for Her X-1, the system can be called a intermediate mass binary (IMXB). Due to the greater relevance for the following analysis a more precise explanation of HMXBs is given. A more detailed explanation of the formation and evolution of the three mentioned types of X-ray binaries, amongst others, can be found in e.g. Tauris & van den Heuvel (2006).

2.1.1 High Mass X-ray Binary (HMXB)

A characteristic property of HMXBs is their predominant mass transfer mechanism. While in LMXBs the mass transfer is usually dominated by Roche lobe overflow, the donor star of the HMXB mainly loses mass due to its stellar wind, which is then accreted by the compact companion of the binary system (Ballhausen, 2021).

These HMXBs usually have short orbital periods that are less than 10 days and a companion with a mass ranging from $18 M_{\odot}$ to $40 M_{\odot}$. Known examples of this type of binary system are Vela X-1, Centaurus X-3 or Cygnus X-1 (van den Heuvel, 2004).

A sub-type of the HMXBs are the B-emission X-ray binaries, or Be X-ray binaries. The characteristic that separates these systems from ordinary HMXBs is the disc of gas that forms

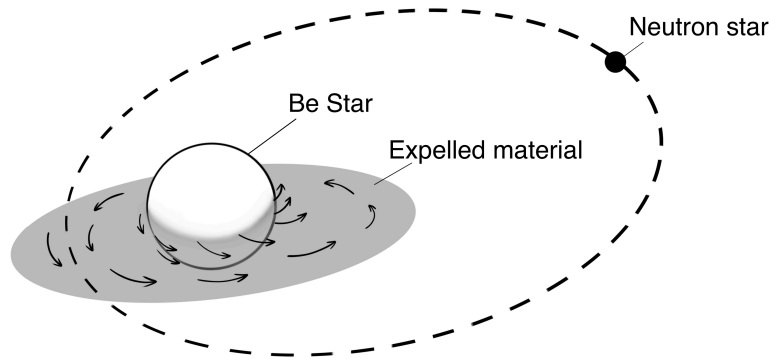


Figure 2.2: Schematic representation of a Be binary system, after van den Heuvel (2004).

around the equator of the B type star, due to its fast rotation. A schematic illustration is shown in Figure 2.2. The orbital periods of these systems are typically longer than for normal HMXBs, ranging from about 15 days to several years. The mass of the companion is in general lower and ranges from $8 M_{\odot}$ to $20 M_{\odot}$. In contrast to the normally persistent X-ray emission of a standard HMXB, Be binary systems are transient sources. That means they only start emitting when their companion ejects mass, forming the equatorial disc of gas. That then enables the neutron star to accrete mass when passing through the disc of the Be star. These mass ejection phases are normally quite irregular and can be separated by years long quiescence (van den Heuvel, 2004).

The observed outbursts can be further classified as the regular “type I” outbursts, or the giant “type II” outbursts. A “type I” outburst happens when the accretor, e.g. a neutron star, passes the point of its orbit that is closest to its donor, the periastron. These outbursts usually have low luminosities of $\sim 10^{36} - 10^{37} \text{ erg s}^{-1}$ (Baykal et al., 2005; Paul & Naik, 2011). Further information on outbursts of the “type I” can be found in e.g. Bildsten (2000). “Type II” outbursts start in general after the periastron passage, but show no other correlation with the parameters of the orbit. They usually have a duration of several weeks to months with luminosities greater than $10^{37} \text{ erg s}^{-1}$, see Finger & Prince (1997) or Baykal et al. (2005). Two example light curves of systems that undergo both type I and type II outbursts are shown in Figure 2.3. It can be seen in both example systems that type I outbursts are observed more regularly. The outbursts of type II happen less frequent, but reach a several times higher peak luminosity.

The work done in this thesis uses data from a giant type II outburst of a neutron star Be X-ray binary system. More information on the specific source are given in chapter 3.

Since the analysis performed in chapter 6 mainly focuses on the observed spectra of the source, further detail about the spectral characteristics is needed. Therefore the following subsections are about spectral features that can be observed in this type of binary system.

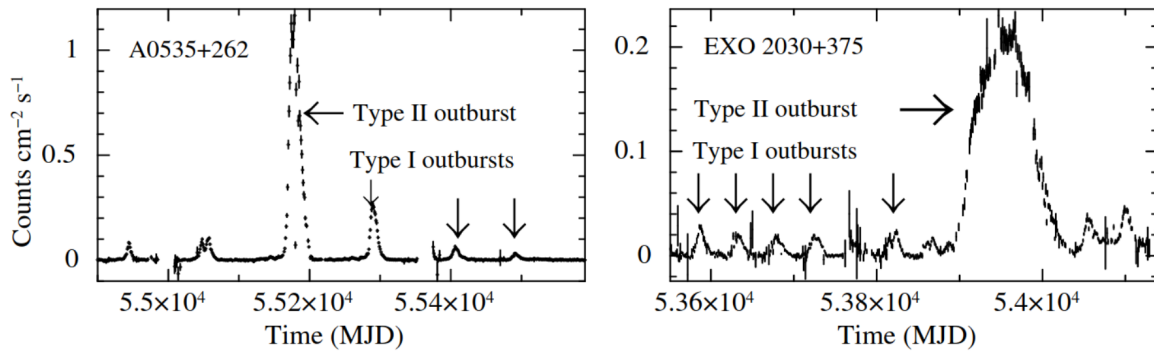


Figure 2.3: Swift/BAT light curves of two different Be/X-ray binary systems, A0535+262 and EXO 2030+375, taken in the energy range from 15 to 50 keV. The different types of outburst are marked in both plots using arrows. Image taken from Paul & Naik (2011).

2.2 Cyclotron Resonant Scattering Features (CRSFs)

Neutron stars are compact objects that can create special physical scenarios in their close surroundings. Aside from high temperatures and a strong gravitational field, they can also have strong magnetic fields with strengths of more than 10^{12} G at the poles. Comparing the magnetic field strengths of neutron stars in binary systems showed that neutron stars in HMXBs usually have a higher magnetic field than the ones located in LMXBs. If the neutron star is located in such a binary system it can produce X-rays by accreting matter from its companion. We can then observe this emitted radiation and use it to gain information on the behavior of matter under extreme conditions that can not be reproduced in our laboratories (Coburn et al., 2002). The resulting spectra enable us to study, e.g., the accretion mechanism onto these objects in detail that we cannot obtain otherwise.

One characteristic property of the neutron star is its Alfvén radius. This is the distance at which the gravitational field of the compact object starts to influence the accreted plasma (Thomson, 2014). After passing the Alfvén radius, the matter that is accreted onto the NS follows the magnetic field lines towards the accretion columns that are located at its magnetic poles.

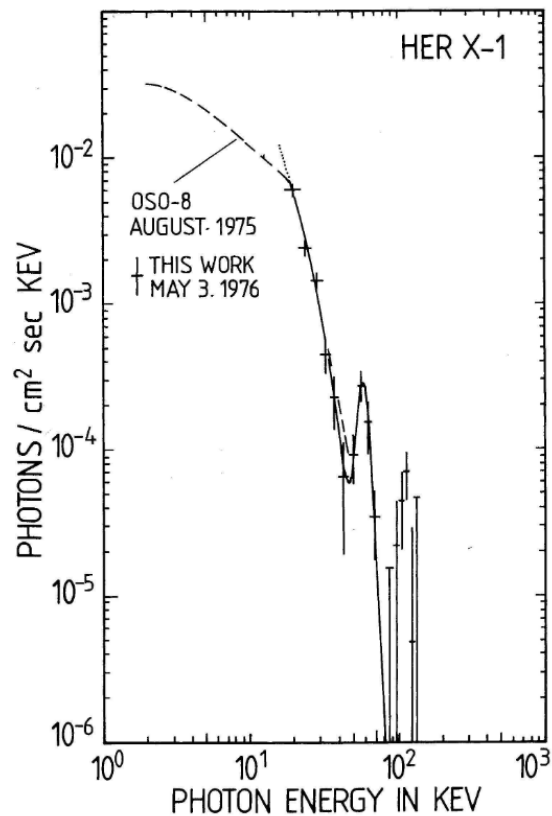


Figure 2.4: First observed CRSF in the spectrum of Hercules X-1, by Truemper et al. (1978).

After passing the Alfvén radius, the matter that is accreted onto the NS follows the magnetic field lines towards the accretion columns that are located at its magnetic poles.

The exact geometry of these columns and the detailed accretion mechanisms are still under debate and several models have been published lately. Some examples are Gornostaev (2021), who uses 3D models to describe the geometry of the accretion column, Zhang et al. (2022), who focus on the column accretion of neutron stars.

Here a more general approach is stated to explain the origin of a spectral feature observed in 4U 0115+63. Inside these columns, thermal photons are created by a hot spot on the magnetic poles of the NS. These photons undergo inverse Compton scattering inside the accretion column. This means that the particle transfers part of its energy to the photon it interacts with. Thereby the photons are up-scattered in energy, creating a spectrum that can be detected in hard X-rays (Müller et al., 2013). Due to the strong magnetic field inside the accretion columns, the energies of the in-falling electrons get quantized along their direction of movement, perpendicular to the magnetic field lines. These discrete energies are called the Landau levels. The electrons also interact with the generated photons, leading to resonant scatterings of the photons of these electrons. The discrete resonance energies thereby create distinct resonance features, called Cyclotron Resonant Scattering Features (CRSFs), also known as cyclotron lines, that can be observed as absorption features in the X-ray spectrum of the NS, see Müller et al. (2013) or Staubert et al. (2019).

The first CRSF was observed in the spectra of Hercules X-1 by Truemper et al. (1978). The original plot showing the respective part of the spectrum, that they published after the discovery, can be seen in Figure 2.4.

The energy $E_{\text{cyc.}}$, that corresponds to the energy difference between neighboring Landau levels, provides information about the strength of the magnetic field at the position where the scattering took place. The relation between the magnetic field B and $E_{\text{cyc.}}$ is given by Coburn et al. (2002) to be

$$E_{\text{cyc.}} = 11.6 \text{ keV} \cdot \left(\frac{B}{10^{12} \text{ G}} \right) \cdot (1+z)^{-1} \quad (2.1)$$

where B is in units of Gauss and z denotes the gravitational redshift.

During the scattering process electrons can be scattered not only from the ground level to the neighboring one, but also to even higher levels. The CRSF that results from a scattering from the ground level to the next higher one is called the fundamental cyclotron line. Scatterings to even higher levels produce harmonic CRSFs that are located at integer multiples of the energy of the fundamental line (Staubert et al., 2019).

If CRSFs can be observed in a system, usually the fundamental line and perhaps one additional harmonic CRSF can be found in the spectrum. Only a small number of systems are known to show more cyclotron lines. The system with the most confirmed CRSFs is the HMXB system 4U 0115+63, that will also be discussed in more detail in chapter 3. In the spectrum of this source a total of 5 cyclotron lines could be verified, with the fundamental line located at ~ 11 keV along with four harmonics (Ferrigno et al., 2009). Another source worth mentioning is the Be/X-ray binary system Swift J1626.6–5156. It has a total of four detected CRSFs and moreover, its fundamental CRSF is located at ~ 4.9 keV. That makes Swift J1626.6–5156 the overall second known accreting pulsar with more than three observed cyclotron lines and the object with the so far lowest known magnetic field of $\sim 4 \cdot 10^{11}$ G (Molkov et al., 2021).

As previously stated the energy of the CRSF allows us to calculate the strength of the magnetic field in the line forming region of the accretion column. In theoretical models, see, e.g., Basko & Sunyaev (1976); Mihara et al. (2004), the energy E_{CRSF} also shows a dependency on the height of the line forming region above the surface of the NS, also known as the characteristic

emission height. This height is said to change with the rate at which the in-falling matter is accreted and with how the matter is decelerated. This should result in a luminosity dependency of the characteristic emission height. Taking these relations into account it is possible that a dependency of the energy of the cyclotron line on the luminosity of the source exists. These theoretical considerations predicted three different possible behaviors: a positive correlation, a negative correlation and no correlation, that could be verified in observational data. Some systems that show a positive correlation between the cyclotron line energy and the luminosity are Hercules X-1 (Staubert et al., 2007), Vela X-1 (Fürst et al., 2014; La Parola et al., 2016) and GX 304–1 (Klochkov et al., 2012; Rothschild et al., 2017). A negative correlation has been observed in V0332+53, see Makishima et al. (1990); Doroshenko et al. (2017); Vybornov et al. (2018) In the third case, the energy of the CRSF is independent of the observed luminosity. This behavior was said to be observed in 1A 0535+262 (Caballero et al., 2007). However more recent publications show a change from a correlation to an anti-correlation, when passing the critical luminosity (Kong et al., 2021).

Another system for which such a correlation is still under discussion is 4U 0115+63. At first the cyclotron line energy of this X-ray binary was said to be anti-correlated with the luminosity (Becker et al., 2012). Later on Müller et al. (2013) proved that the observability of this correlation depends on the chosen continuum model. This behavior is also discussed in more detail in chapter 3.

The measured energies of the respective fundamental CRSF of different systems, plotted over the luminosity of the respective observation, are shown in Figure 2.5.

2.3 Quasi-periodic oscillations (QPOs)

A feature that can be observed in the light curves of NS binary systems are quasi-periodic oscillations (QPOs). QPOs can be detected in the emitted radiation of, e.g., neutron stars or black holes and show up as a recurring brightening in the light curve. Since the times between the occurrences of these intensity peaks can vary slightly, no exact frequency can be determined. Therefore these oscillations are called quasi-periodic, see Thomson (2014).

One way to determine an approximate frequency of a QPO is by determining power density spectra. In this way the QPOs appear not as a narrow peak at one distinct frequency, but as a broadened feature, see Figure 2.6. The figure shows the power density spectra of three different pointed observations. It can be seen that the determined QPO frequency varies slightly.

These luminosity fluctuations were first observed some decades ago, with one of the first being the 0.062 Hz pulsation found in the observations of a flare of 4U 0115+63 (Soong & Swank, 1989).

Depending on their frequency, QPOs can be subdivided into low-frequency QPOs, with frequencies ranging from several mHz up to ~ 60 Hz, and high frequency QPOs, starting at a few hundred Hz up to more than one kHz. The QPOs with the highest frequencies are also known as kHz QPOs (Motta et al., 2017).

The origin of these peaks in the light curves of XRBs is still unknown, but several possible explanations are given in the literature, see e.g. Paul & Naik (2011) (for HMXBs) or Motta et al. (2017) (for LMXBs).

Since 4U 0115+63 is a HMXB, the following explanations focus on this type of binary system. As stated by Ding et al. (2021), two models are most widely-used to describe QPOs in HMXBs. The first one is the Keplerian Frequency Model (KFM), described by e.g. van der Klis et al.

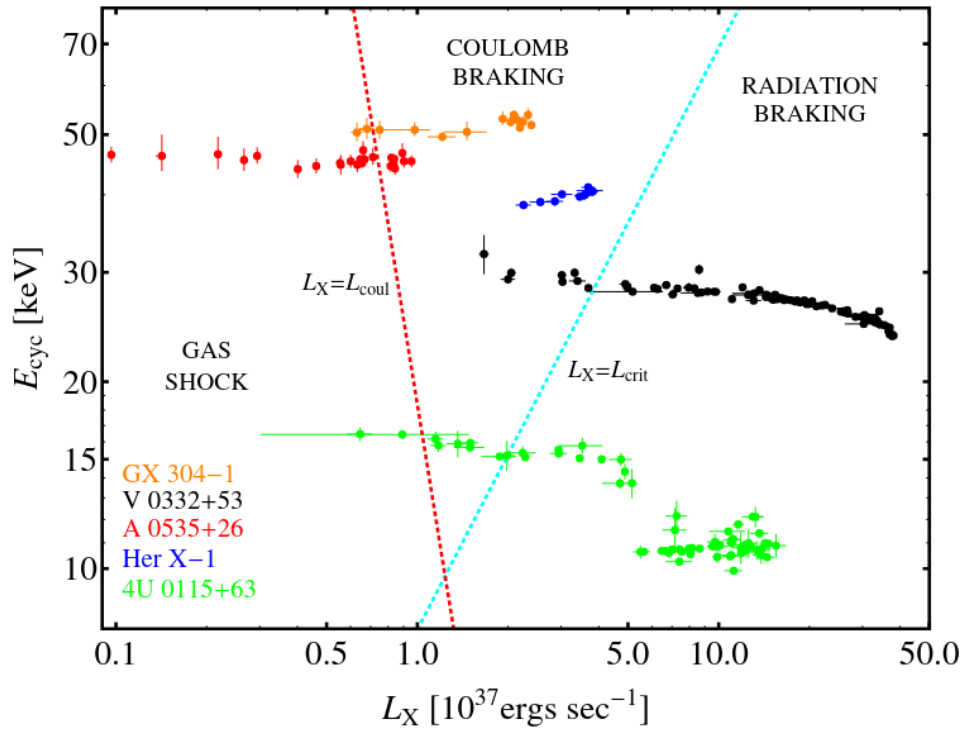


Figure 2.5: Measured cyclotron line energies of different sources at different luminosities. The data was taken on long-term timescales. The dashed lines correspond to the cases where the luminosity L_X equals the Coulomb stopping luminosity (red) and the critical luminosity (blue), respectively. Image taken from Becker et al. (2012). One can also find more detailed information there.

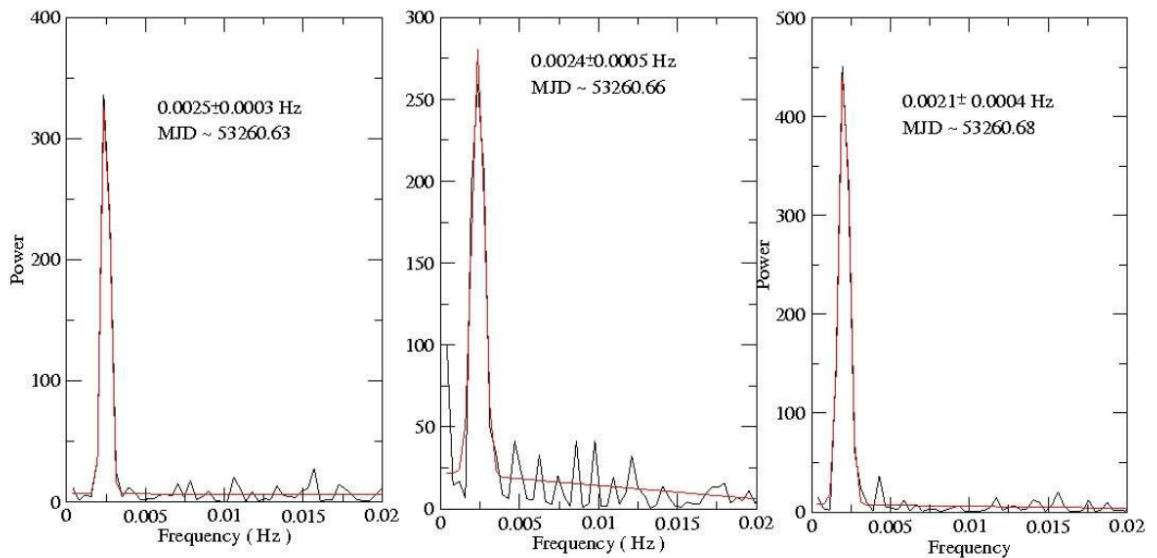


Figure 2.6: Power density spectra of three different pointed INTEGRAL observations of 4U 0115+63. Image taken from Blay (2010).

(1987). It proposes that the QPOs are caused by inhomogeneities in the inner part of the accretion disc at the highest stable rotation frequency of the star (Keplerian frequency). The second model is the Beat Frequency Model (BFM), see e.g. Alpar & Shaham (1985). There the QPOs originate from the deviation of the spin frequency of the inner part of the accretion disc from the Keplerian frequency.

Among the observed X-ray pulsars only a small number of systems are known to show both CRSFs and QPOs. Out of 36 persistent and transient X-ray binary sources that have at least one detected CRSF, only 10 also have QPOs (Raman et al., 2021). A list of these ten known sources is given in Table 2 of Raman et al. (2021).

2.4 The 10 keV feature

As detectors became more sensitive, more detailed spectra could be observed. Therefore, models used to describe the spectra also had to become more precise. However sometimes increasing the complexity of the functions, e.g. from a simple power-law to a power-law with an high energy cut-off, was not sufficient. As the observations got more detailed different spectral components could be resolved in the observations that needed to be modeled using a combination of several functions. The origin of some of the previously observed features, e.g. the CRSFs that were discussed in section 2.2, can now also be explained theoretically. These descriptions then provided us with additional information about the system. An example is the magnetic field strength close to the surface of the neutron star that can be obtained from the energy of the fundamental CRSF. However some other observed spectral features still remain unexplained.

Some NS binary systems show an additional spectral feature that is mostly observed in emission, as in 4U 0115+63, but can sometimes also be detected in absorption, as e.g. in the case of Vela X-1. In general some example systems are 4U 0115+63 to be discussed further in chapter 3, Centaurus X-3 (Suchy et al., 2008), Hercules X-1 (Vasco et al., 2013) and Vela X-1 (Fürst et al., 2014). Due to the location of this extra component typically around 10 keV and the lack of additional characteristics, it was called the “10 keV feature”. In most cases this extra component can be modeled using a black body. However in some cases this additional spectral feature can only be described using a Gaussian absorption or emission feature. Bissinger né Kühnel et al. (2020) compared both approaches and modeled the “10 keV feature” of 4U 0115+63 using both a Gaussian feature and a black body approach. They find that the black body is not sufficient to describe this feature and leads to strong residuals at energies below 10 keV. This can be attributed to the different shapes of the individual spectral components. A comparison of the contribution of a 8.5 keV Gaussian and a black body with $kT = 2.7$ keV is shown in Figure 2.7. Both components have the same total flux, but the energy distribution is significantly different. While the black body provides a more even contribution over a wide energy range the Gaussian peaks at ~ 10 keV. Bissinger né Kühnel et al. (2020) came to the conclusion that the “10 keV feature” in 4U 0115+63 can not be compared to the additional black body components detected in other sources. They state that this comparably strong contribution of this additional component might hint at a specific physical origin. Bissinger né Kühnel et al. (2020) propose cyclotron cooling as a possible origin of the “10 keV feature”. Since the origin of this feature is still unknown, some other possible explanations are given in the following.

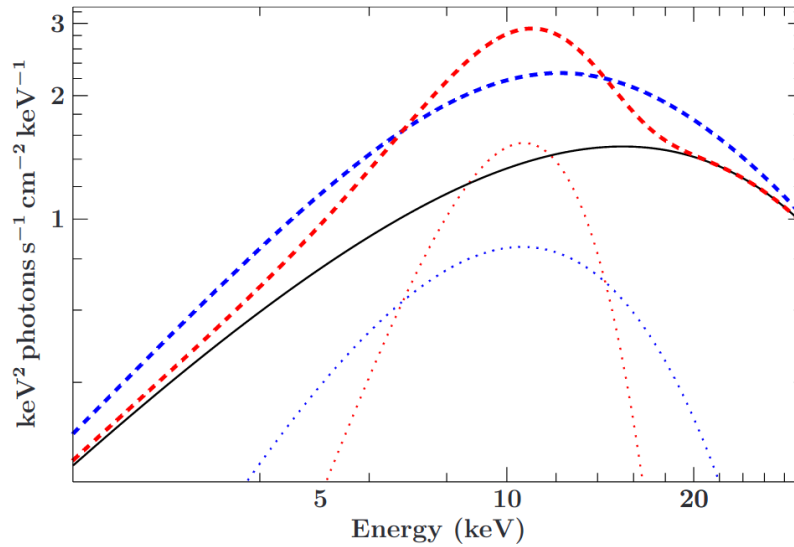


Figure 2.7: Comparison of the contribution of a 8.5 keV Gaussian (red) and a $kT = 2.7$ keV black body (blue) to continuum modeled using a cut-off power-law (solid black line). For both components the same total flux was used. The dotted lines show the exclusive contribution of the black body and the Gaussian. The dashed lines represent the combined spectra of the continuum with the respective additional component. It can be seen that the Gaussian provides a more localized contribution to the fit than the black body. Image taken from Bissinger né Kühnel et al. (2020).

The “10 keV feature” could be an additional emission component of thermal nature. This potential black body emission could originate from the surface of the neutron star. However a more suitable theory to explain the origin of these extra thermal component would still be needed.

Another approach to explain the “10 keV feature” is that it might result from a more complex formation mechanism needed to explain the overall shape of the fundamental CRSF. An example of how relativistic cross sections affect the shape and the energy of the cyclotron line is discussed in Alexander et al. (1989). As stated in section 2.2 the cyclotron lines are formed by the scattering of photons. This scattering process leads to a redistribution of the photons in energy and their direction of movement. The photons are shifted towards lower energies, resulting in a broad red wing of the fundamental CRSF. Since in case of 4U 0115+63 the “10 keV feature” is located at ~ 7 keV and the fundamental cyclotron line is observed at ~ 11 keV a possible shift to lower energies could describe the location of the “10 keV feature”. The comparably low energy of the fundamental CRSF could then also explain the relatively low energy of the observed “10 keV feature”.

On one hand the photons can interact with thermal electrons. This thermal comptonization leads to an upscattering of the photons that results in a broadening of the CRSF. On the other hand bulk comptonization is possible, where the photons interact with the infalling electrons. Both of these processes can create a more complex formation of the CRSF and the continuum. The infalling particles can also collide with the ambient electrons of the accretion column. This can lead to a collisional excitation of the electrons to higher Landau levels. The excited electrons then radiatively decay back and thereby emit photons with energies close to the energy of the fundamental CRSF. These photons can be further reprocessed in the plasma

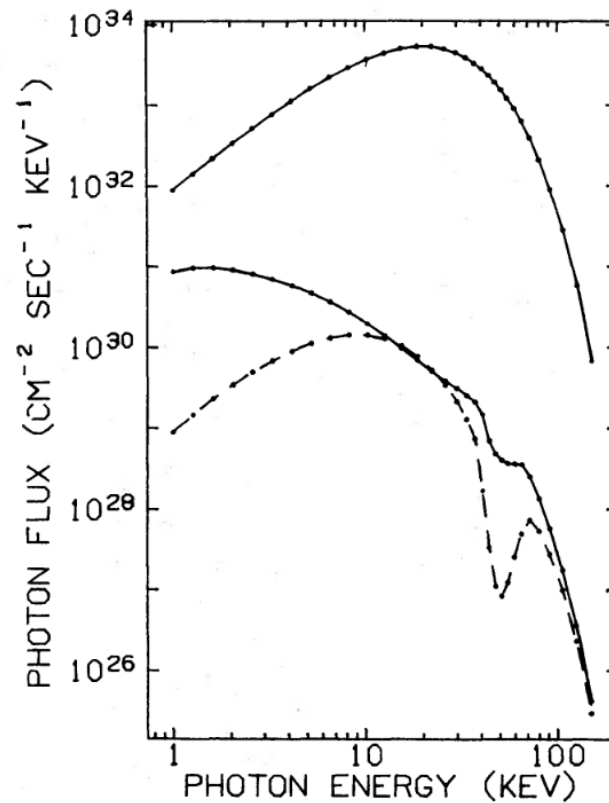


Figure 2.8: Photon fluxes of ordinary mode photons (solid line) and extraordinary mode photons (dashed line) from a strongly magnetized, hot plasma. The third and uppermost line shows the Wien spectrum, that is applied when describing the spectrum of thermal radiation. Image taken from Nagel (1981).

leading to a possible additional spectral component (Nelson et al., 1993, 1995). However so far there are no explicit hints for this potential asymmetry of the harmonic CRSFs in 4U 0115+63 (Sokolova-Lapa E. priv. comm.).

Another approach focuses on the differences in the formation of the diverse spectral components in a highly magnetized plasma, as described by radiative transfer models. One example is the photon flux of different polarization modes. As can be seen in Figure 2.8 the shape of the determined photon flux shows a clear disparity over photon energies ranging from 1 to 100 keV (see Nagel, 1981, for detailed examples). During observations the contributions from these different modes cannot be viewed individually. Since only the combined signal can be measured, the shape of the resulting spectrum then might deviate from an expected overall power-law like continuum (Sokolova-Lapa E. priv. comm.).

Chapter 3

4U 0115+63

For this analysis the HMXB system 4U 0115+63 was selected due to its characteristics, that were briefly mentioned previously and which will be further specified in this subsection. Furthermore it is one of the best studied systems of its kind that was observed with multiple instruments over the last decades.

The system was first observed by the satellite *Uhuru* in 1979, as reported by Giacconi et al. (1972). This HMXB system consists of an optical counterpart, the Be-star V635 Cas, and a neutron star as its companion (Unger et al., 1998; Negueruela & Okazaki, 2001). 4U 0115+63 is located at a distance of ~ 7 kpc (Negueruela & Okazaki, 2001), has an orbital period of 24.316 d and an eccentricity of $e = 0.34$ (Rappaport et al., 1978). The spin period of the neutron star was determined by Ding et al. (2021) to be $3.613\,98 \pm 0.000\,02$ s. The system undergoes type II outbursts every 3 to 4 years, as can be seen in the daily binned *Swift/BAT* light curve of 4U 0115+63 that is shown in Figure 3.1. The most recent outbursts occurred in the years 2008, 2011, 2015 and 2017 lasting one to two months. The light curve of the 1999 outburst of 4U 0115+63 taken with the *RXTE/All-Sky Monitor* is shown in Figure 3.2. The vertical lines in the plot mark the periastron passage of the system and clearly show that this type II outburst started after one of these periastron passages.

For this analysis observations taken with *NuSTAR* and *Swift* during the 2015 outburst are studied. Further information on these satellites and their optics are given in chapter 4.

Additional to these outbursts and small oscillations of the light curve with the spin period of 4U 0115+63, the system shows strong QPOs with a period of ~ 600 s (Heindl et al., 1999). As shown in Berger (2019), the period of the QPOs could not be determined in more detail. One limiting factor are the repeated gaps in the *NuSTAR* light curve due to the orbit of the satellite. The second complication is the varying shape of the QPO peaks. The observed shapes range from strong distinct peaks to occasional double-peaked structures. Part of a light curve, observed with *NuSTAR* in 2015, displaying the QPOs is shown in Figure 3.3. It is also stated by Heindl et al. (1999), that this ~ 2 mHz QPO can not easily be described using one, or a superposition of multiple, Lorentzian lines, due to its complex and asymmetric shape. Two possible explanations for this QPO are given by Heindl et al. (1999). The first one states that matter from an accretion disc might obscure the beam. The second theory claims that the accretion flow of the matter is not constant, but might be modulated. Previous publications have also taken into account that 4U 0115+63 might have multiple QPOs with different periods, see e.g. Heindl et al. (1999).

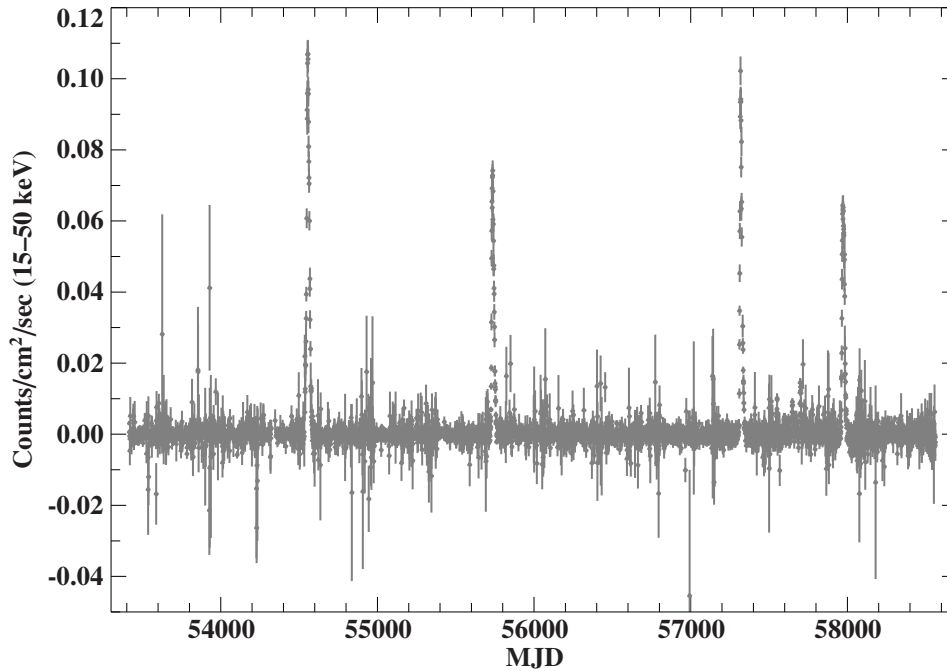


Figure 3.1: Long-time *Swift*/BAT light curve of 4U 0115+63, with daily binning.

An additional unique characteristic of 4U 0115+63 is that the spectrum shows a total of 5 CRSFs, the fundamental line with a centroid energy of ~ 11 keV and four harmonics (Ferrigno et al., 2009; Boldin et al., 2013). In the following analysis 4 out of these previously verified CRSFs could be detected and were included in the analysis. As can be seen in Figure 3.4 Heindl et al. (2000) fitted the spectra, observed during the 1999 outburst of 4U 0115+63, using different numbers of cyclotron lines. They already found that for their data set a total of five CRSFs best described the observation.

Another approach on modeling the CRSFs was followed by Iyer et al. (2015) who analysed several pointed observations, taken with different X-ray satellites, during the 2011 outburst of 4U 0115+63. In this publication the authors claim to have detected a CRSF at ~ 16 keV. This potential CRSF is not a harmonic of the fundamental line at 11 keV, but is said by Iyer et al. (2015) to be an additional fundamental CRSF. This would result in two separate sets of absorption lines that might originate from different regions. Iyer et al. (2015) discuss two possible locations of these regions. First they state that the regions could be located in the same column above one pole, but are located at different heights. They also state that in this case one set of CRSFs might originate in the pencil beam, while the origin of the second set is the fan beam. The second approach is that the two sets of CRSFs might originate from different poles that are located on opposite sides of the neutron star. The possibility that the two sets of CRSFs are created in the same column at different heights was further studied by Liu et al. (2020). They used two *NuSTAR* observations of the 2015 outburst and tried to model the data. However they also mention that this additional CRSF at ~ 16 keV might be connected to the “10 keV feature”. This second fundamental line can only be observed when no additional Gaussian component to model the “10 keV feature” is used.

Thus the existence of two fundamental CRSFs could not be verified. This theory was also discussed in Bissinger né Kühnel et al. (2020). There they used the same *Suzaku* data as Iyer et al. (2015) and redid their spectral fit. This reassessment of the observations showed that

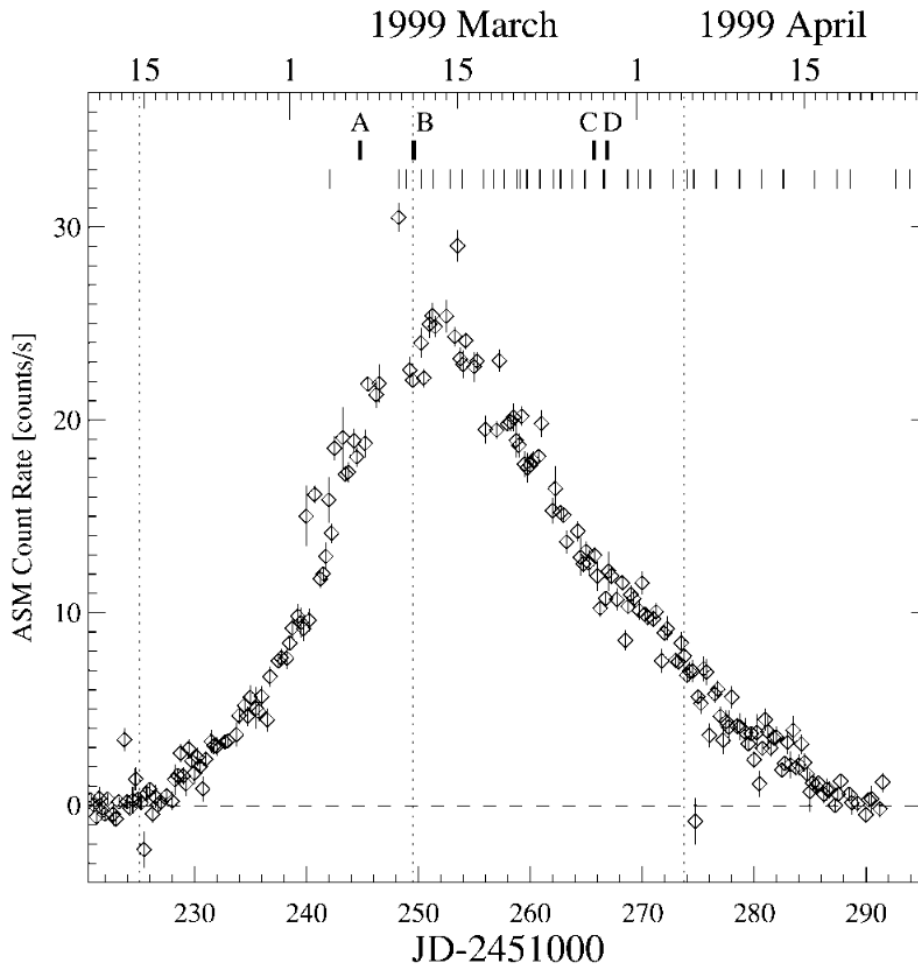


Figure 3.2: Light curve of the 1999 outburst of 4U 0115+63 taken with the *RXTE*/All-Sky Monitor (1.5–12 keV) using 6 h binning. The thick black lines at the top (A - D) mark the times of four additional, long pointed observations. The periastron passages of the neutron star are marked using the vertical dotted lines. Image taken from Heindl et al. (1999).

the previous fit wrongly modeled part of the continuum when fitting the CRSFs. Bissinger né Kühnel et al. (2020) state that no evidence for the second fundamental cyclotron line can be found.

Previous publications also claimed to have found an anti-correlation between the X-ray flux of 4U 0115+63 and the energy of its fundamental CRSF (Nakajima et al., 2006; Mueller et al., 2010; Becker et al., 2012). This theory was disproved by Müller et al. (2013). They showed that this anti-correlation strongly depends on the model used to describe the continuum. The previously observed anti-correlation disappears completely when using an absorbed power-law with a high energy cut-off and an additional Gaussian emission feature to account for the “10 keV feature”. An example fit to a *BeppoSAX* spectrum of the 1999 outburst of 4U 0115+63 can be seen in Figure 3.5. There Ferrigno et al. (2009) used a power-law with an high energy cut-off a broad Gaussian and five CRSFs to describe the spectrum. The contributions of the cut-off power-law and the Gaussian feature to the fit are shown using a dashed and a dot-dashed line respectively. Bissinger né Kühnel et al. (2020) also used the model of Müller et al. (2013)

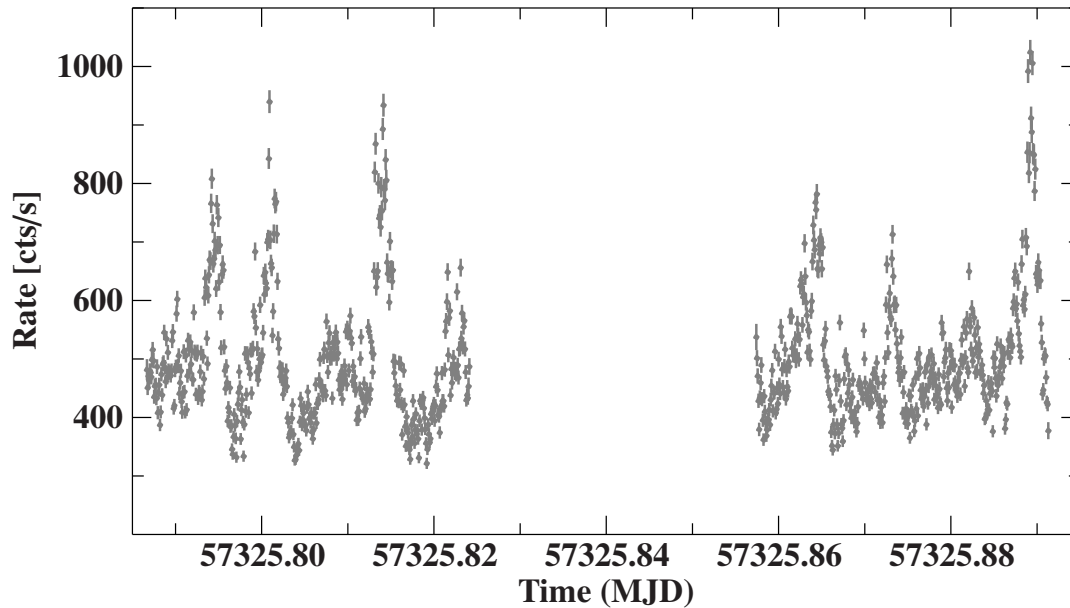


Figure 3.3: Section of the *NuSTAR* light curve of 4U 0115+63, observed during the declining phase of the 2015 outburst. It can be seen that the shape and intensity of the individual QPO peaks varies. The gap in the observation results from the orbit of *NuSTAR* that limits the visibility of 4U 0115+63.

to describe the spectra of 4U 0115+63, but could neither confirm nor disprove the statement of Müller et al. (2013) due to a gap in the *Suzaku* data. Instead they calculated 2 dimensional confidence contours between the energy of the fundamental cyclotron line and its depth and compared these to the results from previous analyses. This approach resulted in the same findings as Müller et al. (2013), supporting their statement of a constant behavior instead of an anti-correlation between the fundamental CRSF energy and the luminosity.

In general 4U 0115+63 is a source that combines many features in its spectrum. In addition these spectral components are also relatively pronounced. In the spectra of most other sources of this type, only one, in some cases two, of the mentioned features (CRSFs, QPOs and a “10 keV feature”) could be detected. This could be because these features are relatively rare, or because our current detectors are not yet able to observe them in other systems.

Therefore the clear observability of these pronounced features: the high number of CRSFs, the strong QPOs and the “10 keV feature”, make 4U 0115+63 a prime example to study these spectral components.

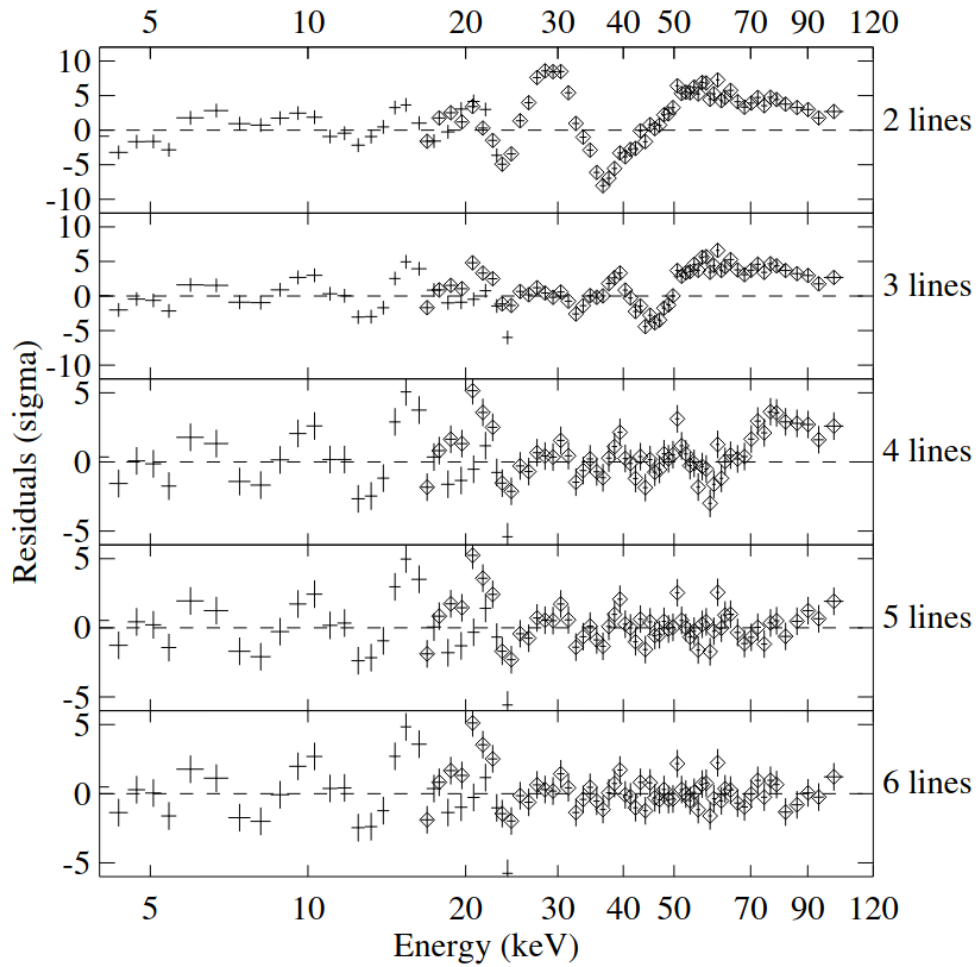


Figure 3.4: Obtained residuals when fitting the *RXTE* data from the 1999 outburst of 4U 0115+63 using a different number of cyclotron lines. The continuum of the spectrum was modeled using Fermi-Dirac cut-off power-law with an additional black body component at low energies. Heindl et al. (2000) identify that the data is best described using five lines. Taken from Heindl et al. (2000).

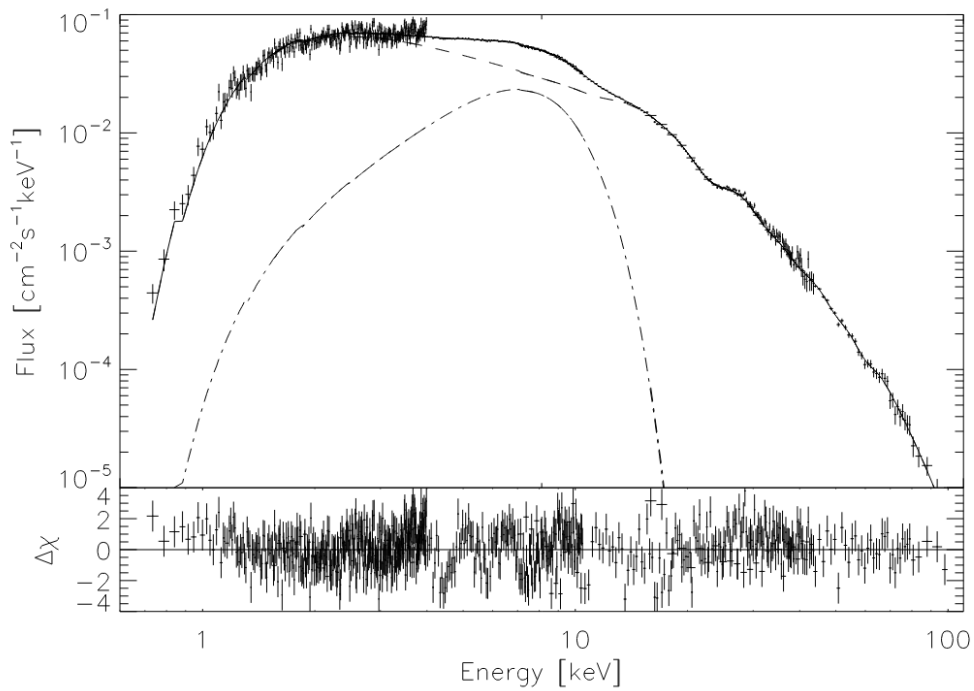


Figure 3.5: *BeppoSAX* spectrum (0.7–100 keV) of the 1999 outburst of 4U 0115+63. The data was obtained by combining observations from four instruments onboard *BeppoSAX*: the *LECS*, the *MECS*, the *HPGSPC* and the *PDS*. The upper panel shows the unfolded spectrum (black data points). The continuum was modeled using a power-law with an high energy cut-off (dashed line) and an additional broad Gaussian (dot-dashed line). The total model is given by the solid black line. The lower panel shows the residuals of the best fit. Taken from Ferrigno et al. (2009).

Chapter 4

Instruments

For the analysis discussed in this thesis, data from *NuSTAR* and *Swift* was used. The technical properties and additional general information of the detectors onboard the satellites are given in this section. First an overview of the utilized optics onboard the satellites is given.

4.1 Wolter-I optics

Since normal lenses, as used when focusing optical light, do not work for X-rays, a different type of optics is needed when working with these frequencies. The design used onboard the satellites *NuSTAR* and *Swift* are conical Wolter-I optics. These optics were only invented a few decades ago, in 1952 by Hans Wolter. He primarily constructed these focusing optics for microscopes, but they are also widely used in astronomy.

In these optics the incoming photons get reflected twice at a high angle of incidence from differently shaped mirrors. While the first reflection takes place on a parabolic shaped mirror, the second mirror has a hyperbolic shape. To increase the collection area of this type of optics, multiple of these mirrors of decreasing diameter are put into one other.

A schematic picture is shown in Figure 4.1.

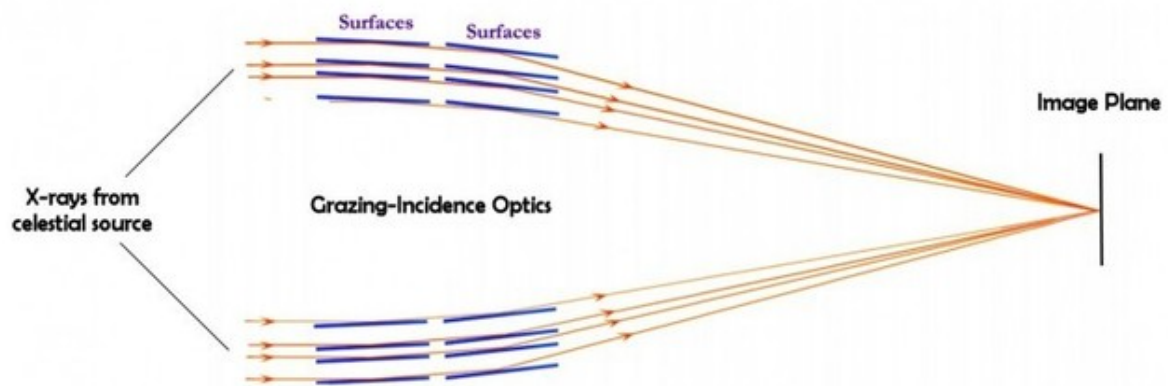


Figure 4.1: Schematic portrayal of the path light takes inside a grazing-incidence optic. Image taken from NuS.

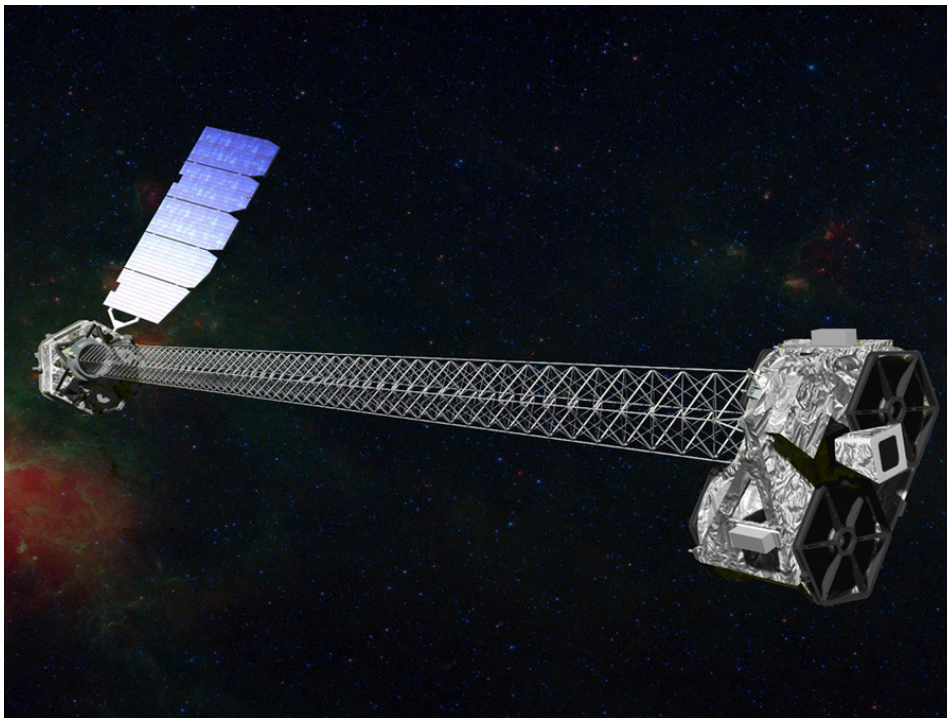


Figure 4.2: Artistic impression of the satellite *NuSTAR* flying in space. Courtesy NASA/JPL-Caltech.

Additional to the requirement that X-rays have to hit the surface of the mirrors at a high angle to not be absorbed, the right surface material for the mirrors is important (NuS).

4.2 The Nuclear Spectroscopic Telescope Array (NuSTAR)

The “Nuclear Spectroscopic Telescope Array” (*NuSTAR*) was launched on June 13th in 2012 and is one of NASA’s small explorers (SMEX) missions. An artistic impression of the spacecraft is shown in Figure 4.2. *NuSTAR* operates in the energy range from 3 to 78.4 keV, with a spectral resolution of 0.4 keV at 10 keV and 0.9 keV at 68 keV, a temporal resolution of $2 \mu\text{s}$, and an angular resolution of $18''$ full width at half maximum (FWHM), see Harrison et al. (2013).

NuSTAR was the first satellite to operate an, at that time, new type of hard X-ray optics, combined with solid-state detectors, enabling it to observe X-rays above 10 keV. A comparison of the effective collecting area of *NuSTAR* and other detectors is shown in Figure 4.3. *NuSTAR* houses two depth-graded multilayer-coated Wolter-I conical approximation optics, see Petre & Serlemitsos (1985) and also Harrison et al. (2013). These optics focus X-rays over a focal length of ~ 10 m onto the two identically manufactured focal plane modules, called FPMA and FPMB. In the case of *NuSTAR* the Wolter-I optics consist of 133 mirrors, with a maximum radius of 191 mm, that were stacked on top of one another. In order to focus X-rays up to nearly 80 keV, multiple layers of Pt/SiC and W/Si were used as a coating for the mirrors, see also NuS. An image of the construction of *NuSTAR*’s optics is displayed in Figure 4.4.

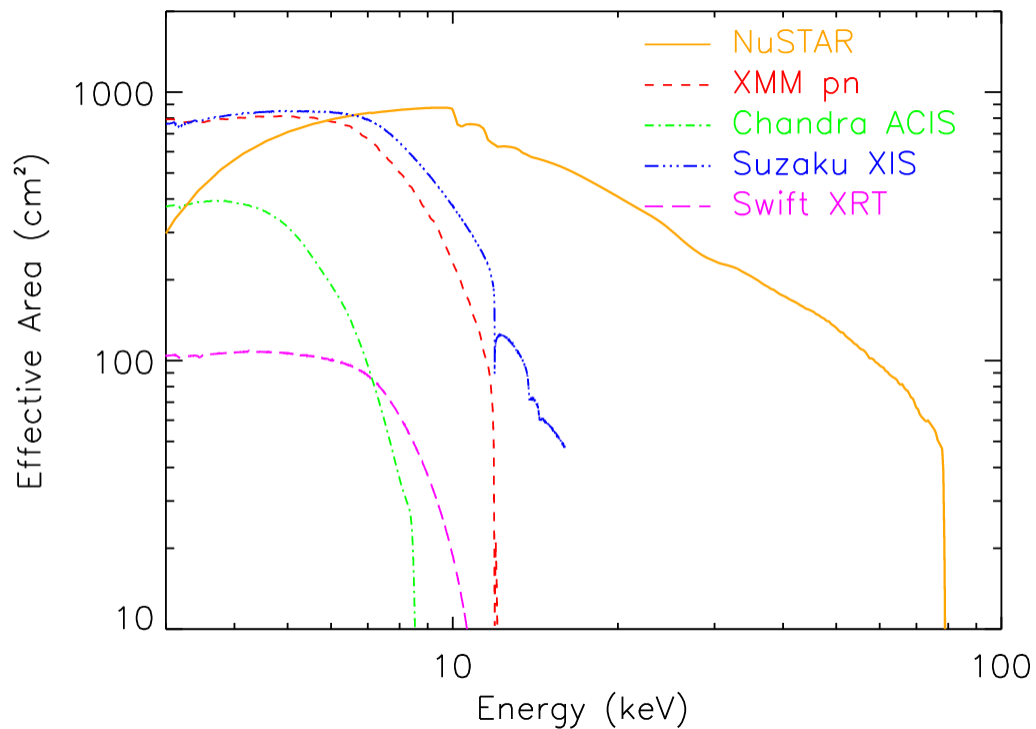


Figure 4.3: Effective area of *NuSTAR* in comparison with the effective collecting areas of some other detectors onboard satellites. To ensure the comparability to *NuSTAR*'s detectors, the CCD detectors onboard *XMM*, *Chandra* and *Suzaku* were used. Image taken from Harrison et al. (2013).

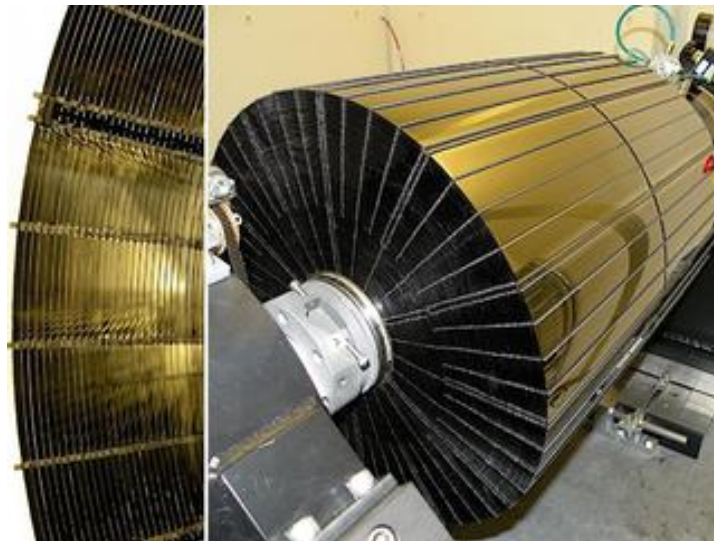
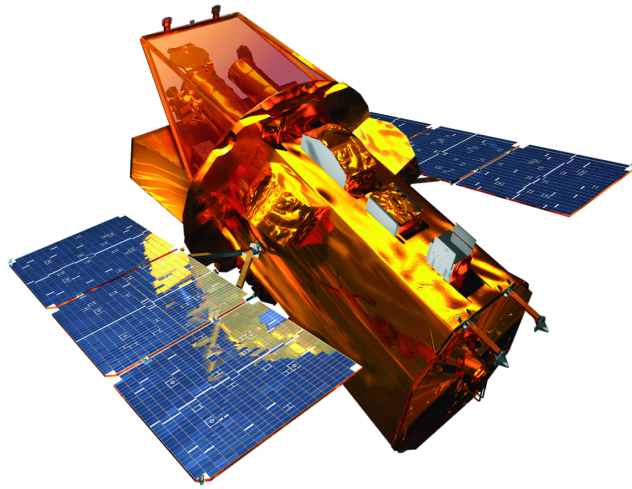


Figure 4.4: On the right the *NuSTAR* optics are shown during its construction at the at Columbia University's Nevis Laboratory. On the left a more detailed image of the layered mirrors is shown. Images taken from NuS.

Each of the two focal plane modules, FPMA and FPMB, consists of four solid-state CdZnTe pixel detectors, that are again sectioned into 32x32 pixels with a side length of 0.6 mm, providing a field of view of 12" (Harrison et al., 2013).

4.3 The Neil Gehrels Swift Observatory (Swift)

The “The Neil Gehrels Swift Observatory” (*Swift*) was launched on November 20 in 2004. It is one of the medium explorer (MIDEX) missions of NASA, with the main science goal being the study of the origin and characteristics of gamma-ray bursts (GRBs). Therefore this multi-wavelength observatory houses three co-aligned detectors that observe at different energies. The largest of the three detectors, the Burst Alert Telescope (BAT), observes in the range from 15 to 150 keV. The Ultraviolet/Optical Telescope (UVOT) takes measurements between 170 and 600 nm. The third instrument, used in this analysis, is the X-ray Telescope (XRT) that measures from 0.3



to 10 keV, overlapping nicely with the higher energy range of *NuSTAR* data (Swi, 2018). An artistic impression of the satellite is shown in Figure 4.5.

Figure 4.5: Image of the satellite *Swift*, generated by a computer (Swi, 2018).

The XRT uses Wolter-I optics with a focal length of 3.5 m to focus X-rays onto a CCD detector that is made of 600 x 600 pixels with a side length of 40 μm . This results in a field of view of 23.6 x 23.6 arcminutes. The optics onboard *Swift* consist of 12 concentric Ni shells, that were coated using gold. These mirror shells have an overall length of 600 mm and varying diameters between 191 and 300 mm. Its energy resolution at launch was 140 eV at 5.9 keV and it has a time resolution of 0.14 ms, 1.8 ms or 2.5 s depending on the utilized mode (Burrows et al., 2005).

The XRT can be operated using different read out modes of the detector. Changing between these modes allows the XRT to fully monitor GRBs, whose flux can vary over several magnitudes during the different evolutionary stages.

The different modes are the Image (IM) mode, the Photodiode (PD) mode, the Windowed Timing (WT) mode and the Photon-Counting (PC) mode. The IM mode is used to determine precise positions and flux estimates. This mode is used when first observing a new target to provide initial position information. The PD mode is used for bright sources with flux between 0.6 Crab and 60 Crab. This fast timing mode provides precise timing information, with an accuracy of 0.14 ms. It can switch between two configurations to adapt to low or high count rates. In WT mode only a section of the total field of view (FOV) of the detector is used. One possible selection is the evaluation of the central 8 arcminutes of the FOV, by using 200 columns of the detector. Next the image is rebinned by combining each ten rows, creating a 1-dimensional image. This mode is appropriate for fluxes between 1 mCrab and 600 mCrab. The PC mode is used for fluxes below 1 mCrab. It observes with a timing resolution of only 2.5 s, but maintains full spectroscopic and imaging resolution (Burrows et al., 2005). More precise information on the different read out modes are given in Hill et al. (2004). The observation analysed in subsection 6.1.1 was taken in the WT mode.

Chapter 5

Observations and data reduction

For the following analysis data taken with *NuSTAR* and *Swift* were used. In this section the chosen observations are introduced. All observations were taken during the giant type II outburst of 4U 0115+63 in the year 2015. The light curve of the outburst, measured using the *Swift/BAT*, is shown in Figure 5.1. A summary of the information on the observations is given in Table 5.1.

Table 5.1: List of the observations used in this analysis. The listed exposure times correspond to the detectors FPMA/FPMB in case of the *NuSTAR* observations and to XRT for observations taken with *Swift*.

	N1	S1	N2	S2
Satellite	<i>NuSTAR</i>	<i>Swift</i>	<i>NuSTAR</i>	<i>Swift</i>
ObsID	90102016002	00081774001	90102016004	00081774002
Start date	2015-10-22	2015-10-23	2015-10-30	2015-10-30
Start time (UTC)	17:30:49	00:17:44	14:01:22	23:26:58
End date	2015-10-23	2015-10-23	2015-10-31	2015-10-31
End time (UTC)	04:01:11	02:12:55	01:21:19	01:18:04
Exposure time [ks]	8.584 / 8.881	2.35	14.564 / 14.898	1.9743
Luminosity [erg/s]	$9.65 \cdot 10^{37}$		$6.23 \cdot 10^{37}$	

NuSTAR observed the system on October 22 and 23 for about 9 ks during the peak of the outburst (ObsID 90102016002, hereafter referred to as N1). The second *NuSTAR* observation took place on October 30 and 31 during the decline, at about half the maximum luminosity, of the outburst and lasted for ~ 15 ks (ObsID 90102016004, N2). The exact positioning of the observations is marked in Figure 5.1 using blue shaded regions. Both data sets were processed using the standard *NuSTAR* extraction pipeline NUSTARDAS version 2.1.2, the HEASOFT version 6.30.1 and the *NuSTAR* calibration database (CALDB) version 20220912. Detailed explanations of the individual steps of the procedure can be found in “The *NuSTAR* Data Analysis Software Guide” (Perri et al., 2021). The respective source regions were circles with a $100''$ radius, that were placed centered over the source. The background regions were also determined to be circles of a $100''$ radius, but were each placed in one corner of the field of view of the respective detector FPMA or FPMB.

The XRT onboard *Swift* also observed 4U 0115+63 simultaneously with *NuSTAR*. During the peak of the outburst, *Swift* observed the source starting on October 23 for about 2 ks (ObsID:

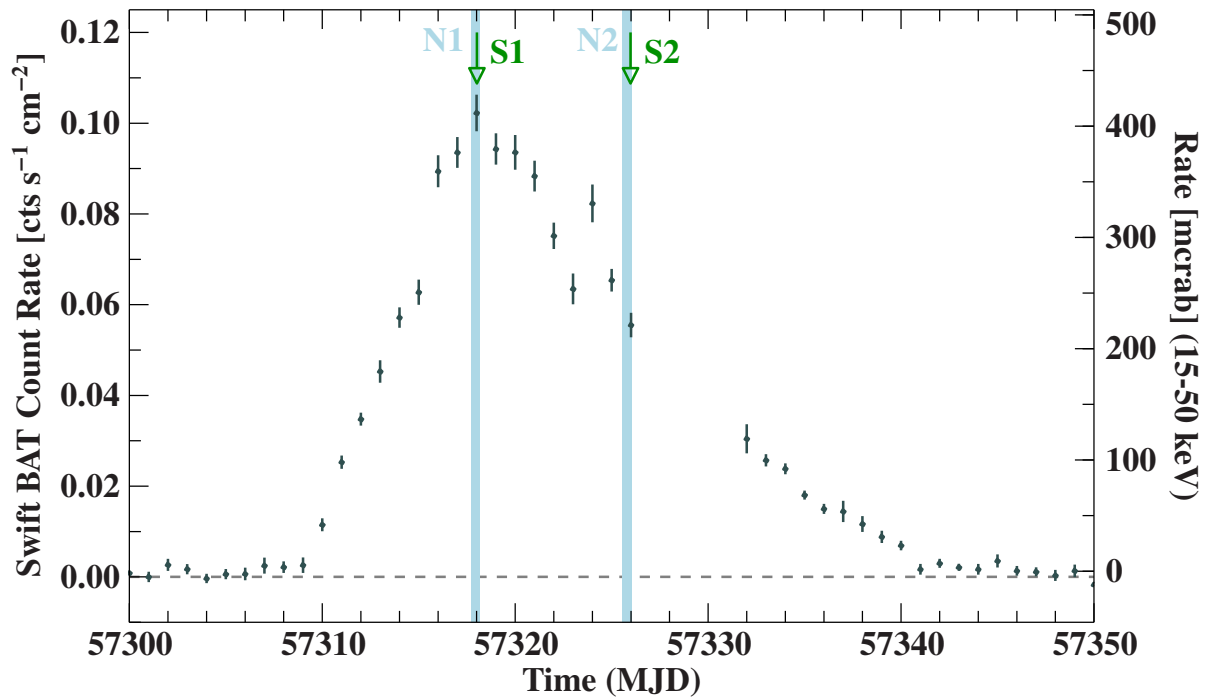


Figure 5.1: The 2015 outburst of 4U 0115+63 as observed with *Swift*/BAT (data points). The blue highlighted regions show the duration of the *NuSTAR* observations, the green arrows mark the start time of the *Swift* observations.

00081774001, hereafter S1). The later observation took place, during the declining phase of the outburst, on October 30 and 31 and lasted also for about 2 ks (ObsID: 00081774002, S2). The start time of both *Swift* observations is marked in Figure 5.1 by the green arrows. The extraction of the spectra and light curves was performed using HEASOFT version 6.30.1 and the *Swift*/XRT CALDB version 20220803. Both observations were taken in the WT mode of the XRT. For the processing of the data sets the *xrtpipeline* XRTDAS was used. Detailed information on the individual processing steps of the pipeline can be found in “The SWIFT XRT Data Reduction Guide” (Capalbi et al., 2005). As source regions rectangular boxes, with a size of 22'' by 40'', were placed over the center of the source. The background regions were each two rectangular boxes, with 25'' by 45'', that were placed at both edges of the observation. All of the following analyses of the spectra and light curves of *NuSTAR* and *Swift* data were performed using the *Interactive Spectral Interpretation System* (ISIS) version 1.6.2-48 (Houck & Denicola, 2000). If not stated otherwise all uncertainties that are listed in connection with the data are given at a confidence level of 90%.

Chapter 6

Data analysis

In this chapter the analysis of the data sets is described. A part of this analysis will also be published in a forthcoming paper.

6.1 Spectral modeling

In the following the fit function, used to describe the spectra, is being discussed.

Since the analysis in this thesis is a continuation of the work done in Berger (2019), the same approach, following the analyses of Müller et al. (2013) and Bissinger né Kühnel et al. (2020), is used when describing the spectra. Detailed information on the utilized functions, e.g. the exact equations, can be found in Arnaud et al. (2022).

As in Berger (2019) a power-law with a high energy exponential cut-off was used to model the overall continuum. The normalization of the function was set to one, while the photon index Γ and the folding energy E_{fold} of the exponential roll-off contribute as parameters to the fit.

To account for the different detectors that were used to measure the spectra, multiplicative cross-calibration constants c_i were added to the fit. The index i thereby indicates the respective detector. The detector FPMA was chosen as a reference. This resulted in $c_{\text{FPMA}} = 1$.

As another multiplicative addition to the fit, N_{H} was added to account for the hydrogen abundance. Here a simplified model was used, neglecting the contributions from elements higher than hydrogen. For the calculations the cross-sections by Verner et al. (1996) and the solar abundance vector by Wilms et al. (2000) were used.

Absorption lines with a Gaussian optical depth were used to describe the CRSFs. The parameters contributing to the fit are the strength D_{CRSF} , the width σ_{CRSF} and the energy E_{CRSF} of the line. In this case the strength D is not the optical depth, that is given by τ_{CRSF} , but can be converted into it by dividing D by $\sqrt{2\pi} \cdot \sigma$. Since the spectrum of 4U 0115+63 shows multiple cyclotron lines, the parameters were further specified by adding a consecutive number to the index. This number was chosen to be 0 for the fundamental line, 1 for the first harmonic CRSF etc.

As discussed in previous works, as for example by Bissinger né Kühnel et al. (2020) and Müller et al. (2013), it can happen that the fit starts modeling part of the continuum using the fundamental CRSF. Additional degeneracies can also appear between the fundamental cyclotron line and the “10 keV feature”. This happens because the energy of this cyclotron line is located close to the energy of the “10 keV feature” and due to their different characteristics. This refers

to the fact that the CRSFs are observed in absorption, while the “10 keV feature” is detected in emission. To prevent the fit from incorrectly modeling the spectrum, the parameters of the CRSFs were constrained. First the energies of the harmonic CRSFs were set to be multiple integers of the energy of the fundamental cyclotron line. Müller et al. (2013) showed that when using a cut-off power-law to describe the continuum of the spectrum with an additional “10 keV feature”, the energies of the harmonic CRSFs deviate only slightly from integer values. This assumption was verified by temporarily fitting a multiplicative constant to the energies. This constant was determined by the fit to be ~ 1.05 . Because the deviation was minor, the multiplicative constant was removed again. As a second constraint, to prevent the fundamental CRSF from getting too broad and thereby modelling part of the continuum, the widths of the cyclotron lines were tied to the energy of the respective line. This was done by stating that the width of the CRSF should be equal to its energy times the multiplicative constant $c_{\text{CRSF},\sigma}$. In previous works the widths of the higher harmonics of the CRSF were often fixed to certain values. However this also limits the potential of the fit to best adapt to the respective spectrum. By using this multiplicative constant the limitation of the fit is reduced without risking unphysical fit parameters that could result when using the CRSFs to wrongly describe part of the continuum.

To model the “10 keV feature”, a broad Gaussian line profile was used. The norm $A_{10\text{keV}}$, given by the total photons/cm²/s in the line, was set to one, while the width $\sigma_{10\text{keV}}$ and the energy $E_{10\text{keV}}$ are fitted.

Furthermore three additional lines with a Gaussian profile were used to model the neutral Fe $K\alpha$ line, the Fe_{XXV} $K\alpha$ line and the Fe_{XXVI} $K\alpha$ line. These lines were chosen based on the analysis of Bissinger né Kühnel et al. (2020). The widths of the individual lines were fixed to 10^{-6} keV. Because of the limited energy resolution of *NuSTAR* around ~ 7 keV the positions of these lines could not be fitted precisely and were therefore also fixed. The energy of the neutral iron line was taken from Kortricht & Thompson (2000), while the energies of the two remaining lines were taken from the AtomDB Atomic Database. If more than one transition contributed to the absorption line the weighted mean of the associated energies was determined. The fluxes of the power-law F_{PL} and the “10 keV feature” $F_{10\text{keV}}$ were also added to the fit. For the calculation the energy range from 3 to 50 keV was used. To gain a measure for the fluxes relative to one another, the ratio $F_{10\text{keV}}/F_{\text{PL}}$ was introduced as a fit parameter.

6.1.1 Combined *NuSTAR* and *Swift* data

In this chapter the analysis of the combined *NuSTAR* and *Swift* observations is discussed. Later, in subsection 6.1.3, the analysis is continued in more detail, using solely the *NuSTAR* observations.

The spectral fit was performed using the model described in section 6.1. In the previous analysis, see Berger (2019), N_{H} had to be fixed at a value of $1.5 \cdot 10^{22}$ cm⁻² due to the lack of data at low energies. After adding the spectra obtained by the XRT onboard *Swift*, and thereby extending the energy range down to 1 keV, this value could also be determined by the fit. The number of fitted CRSFs could also be increased, from three cyclotron lines, to a total of four absorption lines. Thus fits with a red. χ^2 of 1.50 for the first set of observations and 1.42 for the later observations were obtained. The resulting best fit parameters of the fit, using the combined *NuSTAR* and *Swift* data, are listed in Table 6.1.

Table 6.1: Best parameters of the spectral fit with confidence limits. For each observation one measurement from *NuSTAR* and *Swift* each was used.

Parameter	Unit	O1	O2
C_{FPMA}		1.00 [†]	1.00 [†]
C_{FPMB}		0.9619 ± 0.0017	0.9731 ± 0.0016
C_{XRT}		0.941 ± 0.012	0.890 ± 0.013
N_{H}	$\times 10^{22} \text{ cm}^{-2}$	1.93 ± 0.07	1.99 ± 0.07
$E_{\text{CRSF},0}$	keV	11.76 ± 0.08	11.71 ± 0.10
$\sigma_{\text{CRSF},0}$	keV	1.25 ^b	1.42 ^b
$D_{\text{CRSF},0}$		$0.182^{+0.025}_{-0.023}$	$0.155^{+0.036}_{-0.030}$
$E_{\text{CRSF},1}$	keV	23.5 ^a	23.4 ^a
$\sigma_{\text{CRSF},1}$	keV	2.50 ^b	2.85 ^b
$D_{\text{CRSF},1}$		$1.05^{+0.14}_{-0.13}$	$1.15^{+0.19}_{-0.17}$
$E_{\text{CRSF},2}$	keV	35.3 ^a	35.1 ^a
$\sigma_{\text{CRSF},2}$	keV	3.75 ^b	4.27 ^b
$D_{\text{CRSF},2}$		1.9 ± 0.4	$2.2^{+0.6}_{-0.5}$
$E_{\text{CRSF},3}$	keV	47.0 ^a	46.8 ^a
$\sigma_{\text{CRSF},3}$	keV	5.01 ^b	5.70 ^b
$D_{\text{CRSF},3}$		2.2 ± 0.9	$1.1^{+1.1}_{-1.0}$
Γ		0.390 ± 0.030	0.40 ± 0.04
E_{fold}	keV	$9.56^{+0.24}_{-0.23}$	$9.33^{+0.28}_{-0.26}$
F_{PL}	$\text{keV s}^{-1} \text{ cm}^{-2}$	$8.77^{+0.15}_{-0.14}$	6.16 ± 0.09
$A_{10\text{keV}}$	$\text{ph s}^{-1} \text{ cm}^{-2}$	1.00 [†]	1.00 [†]
$E_{10\text{keV}}$	keV	$6.84^{+0.17}_{-0.18}$	7.53 ± 0.12
$\sigma_{10\text{keV}}$	keV	3.75 ± 0.11	3.23 ± 0.08
$F_{10\text{keV}}$	$\text{keV s}^{-1} \text{ cm}^{-2}$	2.59 ^c	1.65 ^c
$A_{\text{FeK}\alpha}$	$\text{ph s}^{-1} \text{ cm}^{-2}$	0.00160 ± 0.00028	0.00113 ± 0.00019
$E_{\text{FeK}\alpha}$	keV	6.40 [†]	6.40 [†]
$A_{\text{FeXXV K}\alpha}$	$\text{ph s}^{-1} \text{ cm}^{-2}$	0.00111 ± 0.00028	$(9.6 \pm 1.9) \times 10^{-4}$
$E_{\text{FeXXV K}\alpha}$	keV	6.69 [†]	6.69 [†]
$A_{\text{FeXXVI K}\alpha}$	$\text{ph s}^{-1} \text{ cm}^{-2}$	$(5.6 \pm 2.6) \times 10^{-4}$	< 0.000323
$E_{\text{FeXXVI K}\alpha}$	keV	6.97 [†]	6.97 [†]
$F_{10\text{keV}}/F_{\text{PL}}$		$0.296^{+0.019}_{-0.018}$	0.268 ± 0.013
$c_{\text{CRSF},\sigma}$		0.106 ± 0.007	$0.122^{+0.011}_{-0.010}$
red. χ^2 / d.o.f.		1.50 / 441	1.42 / 439

(†) Fixed.

(a) Set to the multiple integer value of $E_{\text{CRSF},0}$.(b) Coupled to the respective CRSF energy via $c_{\text{CRSF},\sigma}$.(c) Coupled to F_{PL} via $F_{10\text{keV}}/F_{\text{PL}}$.

This best fit to N1 and S1 is visualized, together with the spectra and the corresponding residuals, in Figure 6.1 (a). The data from FPMA onboard *NuSTAR* is plotted in red, FPMB in blue and data from *Swift* XRT in green. The second fit, using the spectra N2 and S2, is shown in Figure 6.1 (b). It can be seen that the residuals, especially for the later set of observations, show some slight bumps at higher energies. These bumps result from the constraint that was placed on the widths of the CRSFs. However removing this restriction lead to a significantly worse fit of the fundamental cyclotron line.

To better visualize the contribution of some of the components of the fit-function, Figure 6.2 shows the contribution of the cut-off power-law (blue), the “10 keV feature” (red) and the combined iron lines (orange) for both sets of observations.

Figure 4 of Müller et al. (2013) also shows the contribution of the “10 keV feature” and the iron lines compared to the overall spectrum using data from the 2008 outburst of 4U 0115+63. The results of this previous analysis are comparable to the findings in Figure 6.2 of this thesis. The advantage of the analysis done here is the higher signal to noise ratio of the more recent observations. This lead to a higher resolution of the illustrated spectra, making it possible to resolve more spectral details, e.g., the asymmetry of the combined iron lines and the visible dips in the model at ~ 23 keV and ~ 35 keV compared to the cut-off power-law. These deviations result from the absorption of the first and second harmonic CRSF.

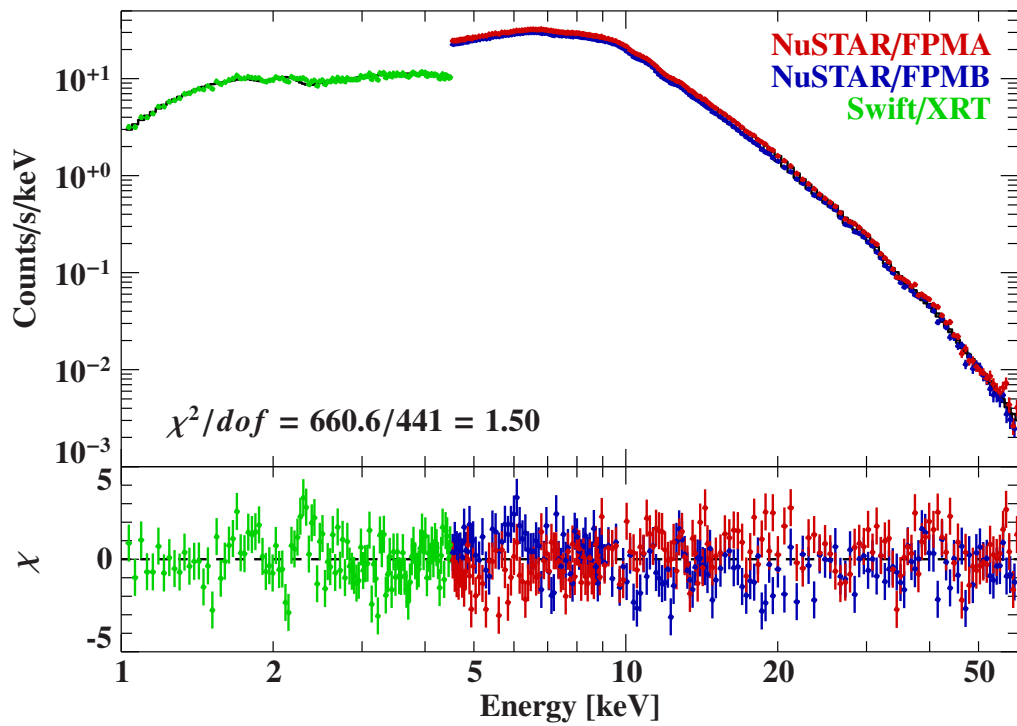
6.1.2 Cross-calibration between *NuSTAR* and *Swift*

For this spectral analysis, *NuSTAR* data in the energy range from 4.5 to 60 keV and *Swift* data between 1 and 4.5 keV were taken into account. The energy ranges were selected this way to avoid problems with the cross-calibration of the satellites that occur when having an overlap in the energies of the data sets. In Figure 6.3 (a) the spectra of N1 and S1 are plotted using more extended energy ranges. Compared to the spectra shown in Figure 6.1 the lower boundary of the energy range of N1 was extended from 4.5 to 3.5 keV. The upper limit of the energy range of the *Swift* observation was extended from 4.5 to 7 keV.

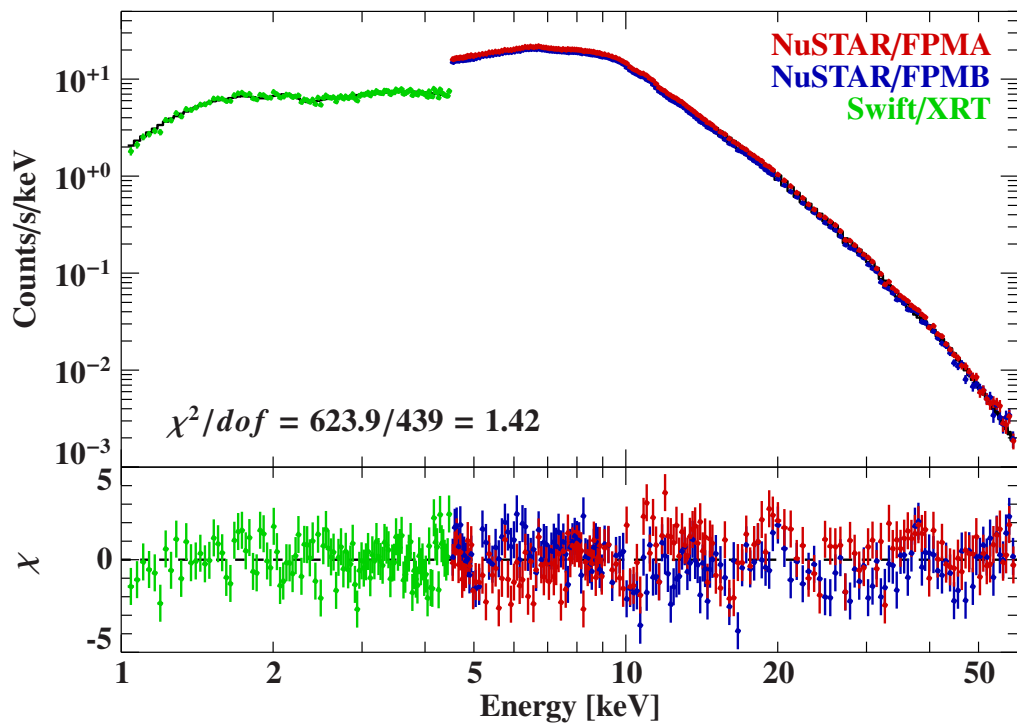
As can be seen in the lower panel of Figure 6.3 (a) the fit, as described in section 6.1, can no longer describe the spectra and the residuals start to increase in the overlapping energy range. The similar behavior can be observed when using observations N2 and S2, see Figure 6.3 (b). This deviation between *NuSTAR* and *Swift* data can also be observed in the spectra of other sources, e.g. GRO J1008–57, MAXI J1535–571 and Swift J1728.9–361, see Madsen et al. (2020).

An explanation of the origin of this behavior can be found in Madsen et al. (2021). There they report on the meeting of the International Astronomical Consortium for High-Energy Calibration (IACHEC) held in November 2020. They discussed updates on the calibration of *NuSTAR* and *Swift* and their cross-calibration. The recordings and slides of these talks can be found on the homepage of the IACHEC. Madsen et al. (2021) state that problems with the cross-calibration in the overlapping energy range from 3 to 5 keV are known for bright sources with an $N_{\text{H}} > 1 \cdot 10^{22}$ which this source has. They also state that up to now no way of solving this problem can be recommended.

A way to reduce the effects of the cross-calibration is to decrease the used energy ranges and avoid an overlap of the spectra. When looking at the residuals of the spectra in Figure 6.3, it can be seen that the increasing slopes cross at ~ 4.5 keV. Therefore this energy was chosen to be the end and starting point of the *Swift* and *NuSTAR* spectra respectively.

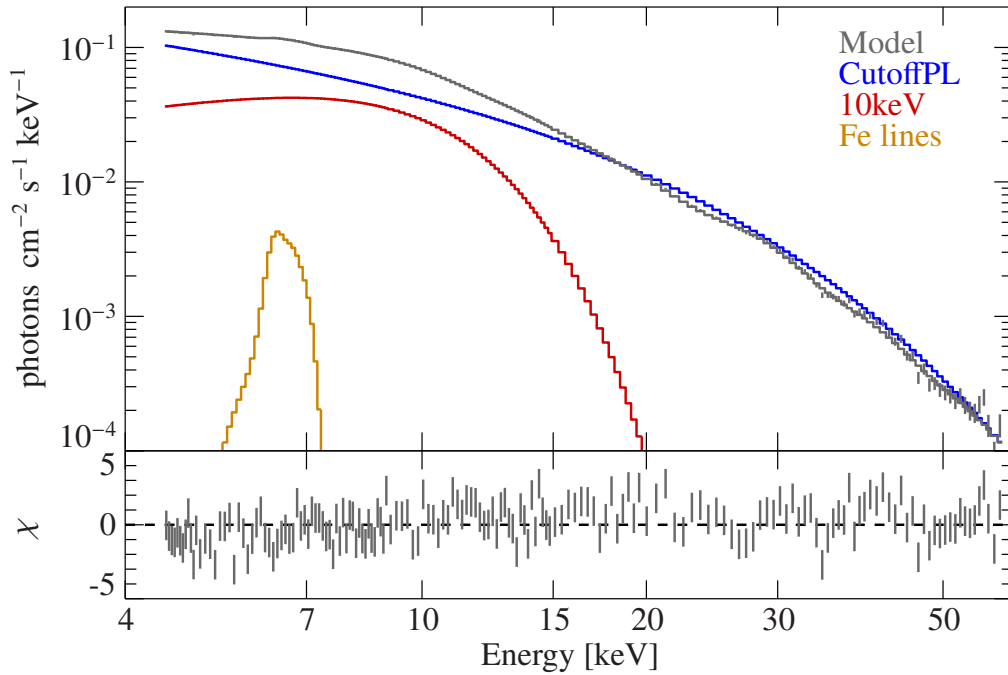


(a) O1

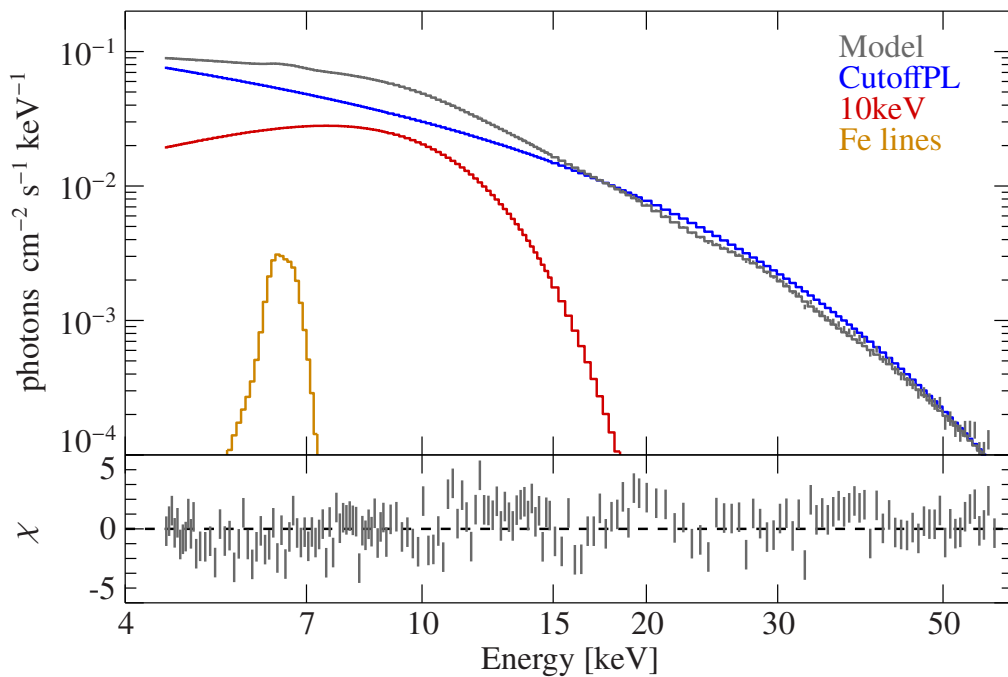


(b) O2

Figure 6.1: Spectra of the simultaneously taken *NuSTAR* and *Swift* observations. (a) uses N1 and S1 while in (b) N2 and S2 are shown. In the respective upper panels the combined *NuSTAR* (FPMA in red and FPMB in blue) and *Swift* (XRT in green) spectra with the resulting best fit are given. The lower panels shows the residuals of the best fit.

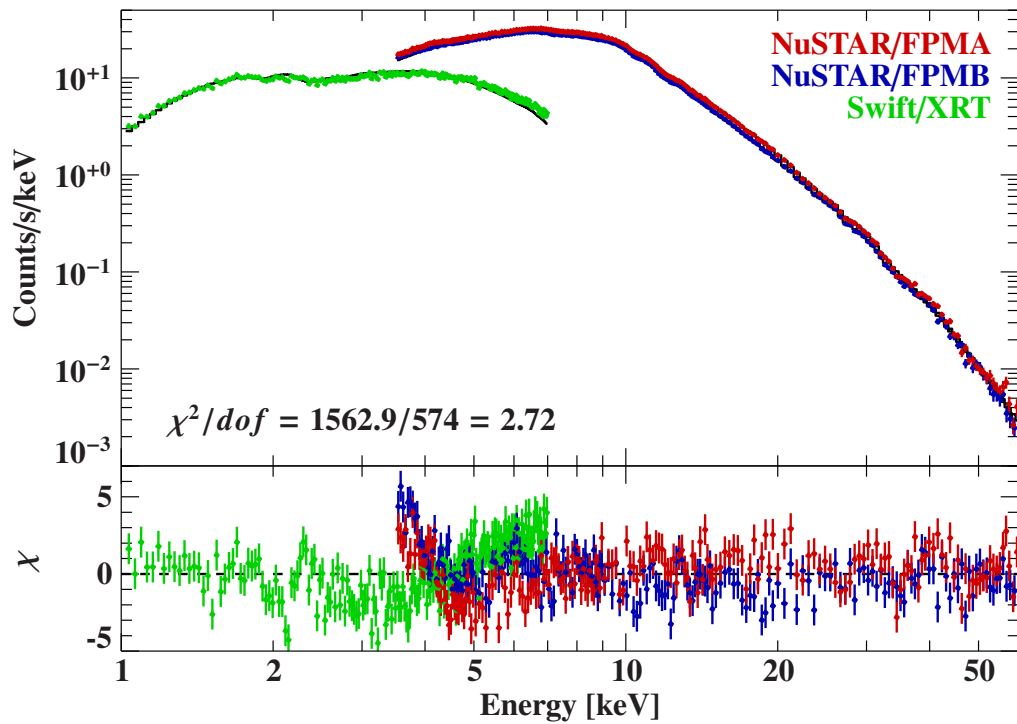


(a) O1

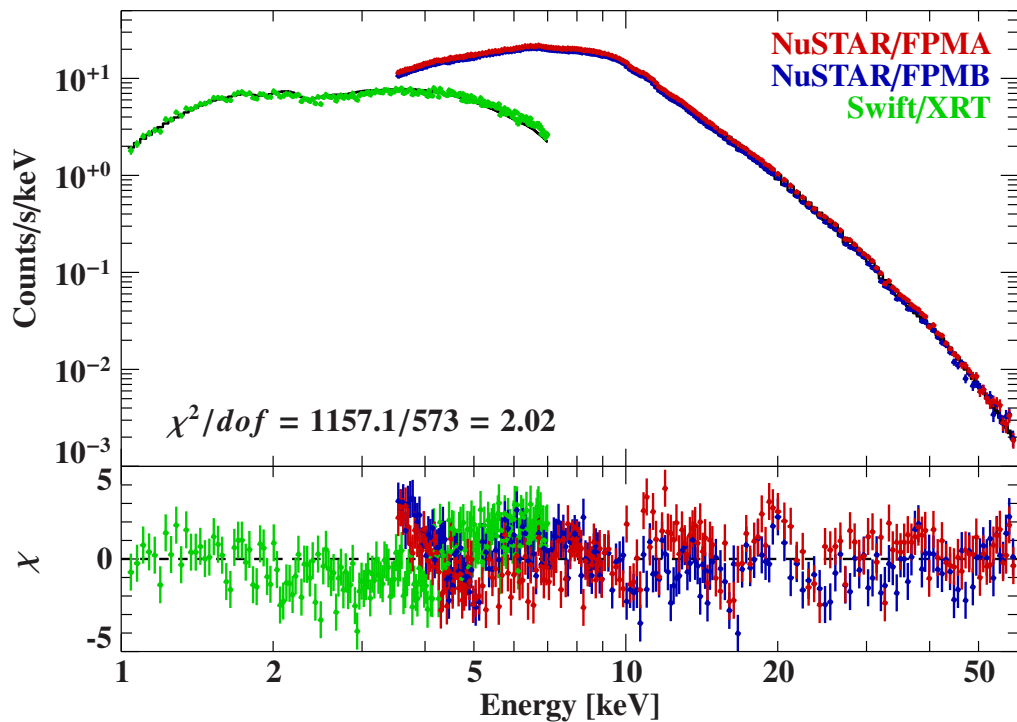


(b) O2

Figure 6.2: Top panels of (a) and (b): Different components of the best fit of the *NuSTAR* and *Swift* observations of are shown, using the energy range of the *NuSTAR* data. The best fit model is plotted in gray, while the contribution of the cut-off power-law (blue), the “10 keV feature” (red) and the combined iron lines (orange) is shown. Lower panels of (a) and (b): Residuals of the best fit parameters of N2 as observed by FPMA.



(a) N1



(b) N2

Figure 6.3: Best fit of the *NuSTAR* and *Swift* observations of O1 (a) and O2 (b) using the extended energy ranges. The lower boundary of the *NuSTAR* observations was changed from 4.5 to 3.5 keV, while the higher limit of the *Swift* observations was moved from 4.5 to 7 keV.

6.1.3 NuSTAR data

This section focuses on the description of the *NuSTAR* data. Similar to the procedure described in the subsection 6.1.1, the fit was performed using the spectral model stated in section 6.1.

The best-fit parameters obtained for both observations N1 and N2 are listed in Table 6.2. Using these parameters resulted in fits with a red. χ^2 of 1.49 for N1 and 1.53 for N2.

Figure 6.4 shows the spectra with the respective best-fit and the corresponding residuals. As in the previous fits, when using the combined *NuSTAR* and *Swift* spectra, bumps can be observed in the residuals around ~ 20 keV and at ~ 40 keV. These bumps arise because of the constraint that was placed on the widths of the cyclotron lines. Again removing this restriction would smooth out the bumps at higher energies, but may also enable the fundamental CRSF to spuriously model part of the continuum. When looking at the determined values for N_H it can be seen that the determined error increased strongly compared to the previous fit. However since the determined value is still close to the previously determined number and did not affect the fit negatively no additional constraint was introduced to the fit and the parameter was not fixed.

6.2 Hardness-Intensity plots

In this chapter the analysis of the hardness ratios (HRs) that was performed in chapter 3.3 of Berger (2019), is continued.

The HRs were calculated using

$$HR = \frac{a}{b}, \quad (6.1)$$

where a and b are the soft and the hard band respectively. For this analysis I continued sectioning the observations into three bands. The soft band s was selected from 3.5 to 5 keV, the medium m energies from 5 to 15 keV and the hard h band from 15 to 50 keV. This partition lead to a total of three different HRs, first s/m , second s/h and lastly m/h .

In Berger (2019) the calculated hardness ratios were plotted over time. This visualization showed no correlation for the s/h HR. On the other hand the HRs including the medium band, that contains the “10 keV feature”, showed variations depending on the count rate of the light curve. When no peak was present in the light curve the both HRs stayed relatively constant and only showed small fluctuations. However during the times when a peak was observed the HR using the soft and medium band s/m seemed to copy the light curve and also peaked at the same time. On the contrary, the HR using the medium and the hard band m/h showed the opposite behavior and dipped at the respective times, compare Figure 11 of Berger (2019).

To further verify this behavior the analysis was continued by plotting hardness-intensity plots for the different HRs of both observations, see Figure 6.5. There the determined HR of a data point is compared to its count rate. For better comparison the respective results for both observations were plotted in the same diagram to better visualize possible differences or similarities. Here data from observation N1 is plotted using gray data point and red error bars. For observation N2 the data points are shown in black with blue error bars.

When comparing the s and the h band the HR stays relatively constant, especially for higher count rates, see Figure 6.5 (b). However when comparing the s and the m band a continuous tendency towards higher HR values for increasing count rates is visible, compare Figure 6.5 (a).

Table 6.2: Best parameters of the spectral fit of both *NuSTAR* observations with confidence limits.

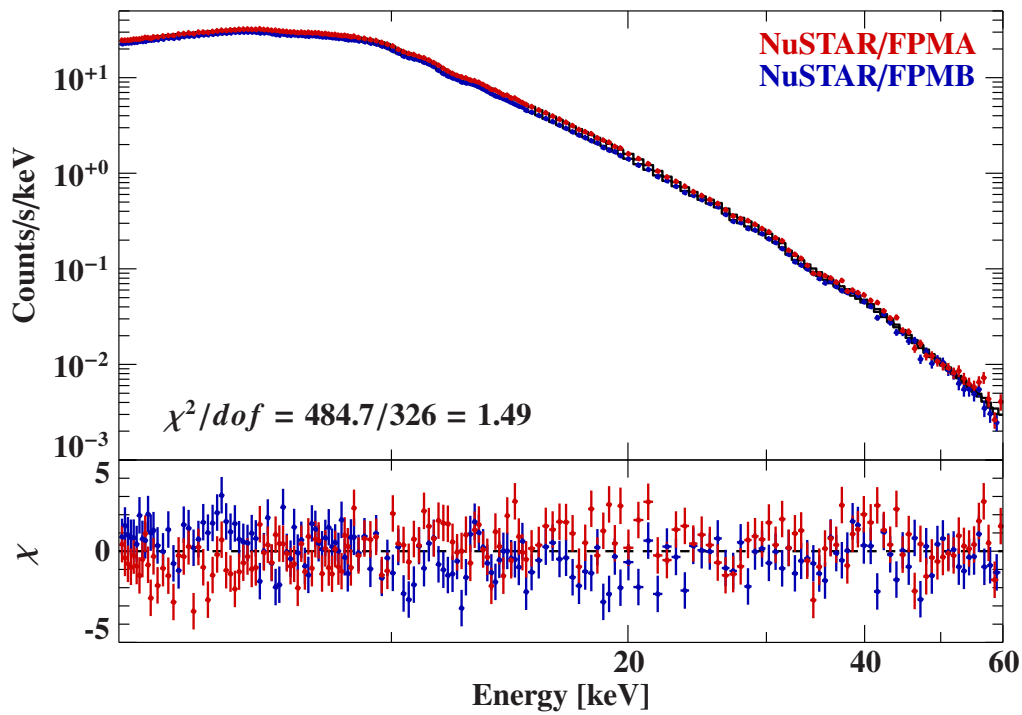
Parameter	Unit	N1	N2
C_{FPMA}		1.00 [†]	1.00 [†]
C_{FPMB}		0.9619 ± 0.0017	0.9732 ± 0.0016
N_{H}	$\times 10^{22} \text{ cm}^{-2}$	2.3 ± 0.8	1.2 ± 0.7
$E_{\text{CRSF},0}$	keV	11.78 ± 0.09	$11.76^{+0.11}_{-0.10}$
$\sigma_{\text{CRSF},0}$	keV	1.23 ^b	1.39 ^b
$D_{\text{CRSF},0}$		$0.173^{+0.028}_{-0.024}$	$0.134^{+0.034}_{-0.029}$
$E_{\text{CRSF},1}$	keV	23.6 ^a	23.5 ^a
$\sigma_{\text{CRSF},1}$	keV	2.45 ^b	2.78 ^b
$D_{\text{CRSF},1}$		$1.01^{+0.14}_{-0.13}$	$1.12^{+0.20}_{-0.18}$
$E_{\text{CRSF},2}$	keV	35.3 ^a	35.3 ^a
$\sigma_{\text{CRSF},2}$	keV	3.68 ^b	4.16 ^b
$D_{\text{CRSF},2}$		1.9 ± 0.4	2.1 ± 0.6
$E_{\text{CRSF},3}$	keV	47.1 ^a	47.0 ^a
$\sigma_{\text{CRSF},3}$	keV	4.91 ^b	5.55 ^b
$D_{\text{CRSF},3}$		2.1 ± 0.9	< 1.88
Γ		$0.37^{+0.06}_{-0.07}$	0.34 ± 0.05
E_{fold}	keV	$9.50^{+0.28}_{-0.27}$	$9.14^{+0.30}_{-0.28}$
F_{PL}	$\text{keV s}^{-1} \text{ cm}^{-2}$	$8.68^{+0.26}_{-0.27}$	6.04 ± 0.12
$A_{10\text{keV}}$	$\text{ph s}^{-1} \text{ cm}^{-2}$	1.00 [†]	1.00 [†]
$E_{10\text{keV}}$	keV	$6.64^{+0.30}_{-0.33}$	7.41 ± 0.15
$\sigma_{10\text{keV}}$	keV	$3.83^{+0.18}_{-0.17}$	3.30 ± 0.09
$F_{10\text{keV}}$	$\text{keV s}^{-1} \text{ cm}^{-2}$	2.69 ^c	1.69 ^c
$A_{\text{FeK}\alpha}$	$\text{ph s}^{-1} \text{ cm}^{-2}$	0.0014 ± 0.0004	0.00119 ± 0.00021
$E_{\text{FeK}\alpha}$	keV	6.40 [†]	6.40 [†]
$A_{\text{FeXXV K}\alpha}$	$\text{ph s}^{-1} \text{ cm}^{-2}$	0.00102 ± 0.00030	$0.00102^{+0.00019}_{-0.00020}$
$E_{\text{FeXXV K}\alpha}$	keV	6.69 [†]	6.69 [†]
$A_{\text{FeXXVI K}\alpha}$	$\text{ph s}^{-1} \text{ cm}^{-2}$	$(4.5 \pm 2.8) \times 10^{-4}$	< 0.000332
$E_{\text{FeXXVI K}\alpha}$	keV	6.97 [†]	6.97 [†]
$F_{10\text{keV}}/F_{\text{PL}}$		$0.310^{+0.033}_{-0.029}$	0.280 ± 0.016
$C_{\text{CRSF},\sigma}$		$0.104^{+0.008}_{-0.007}$	$0.118^{+0.011}_{-0.010}$
red. χ^2 / d.o.f.		1.49 / 326	1.53 / 325

([†]) Fixed.

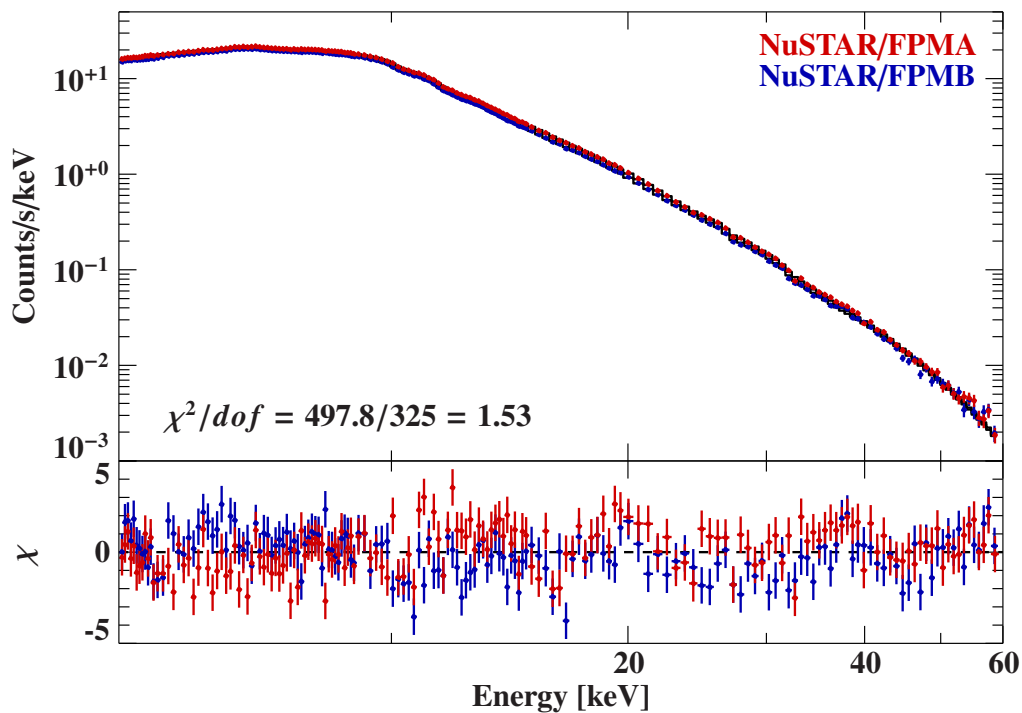
(^a) Set to the multiple integer value of $E_{\text{CRSF},0}$.

(^b) Coupled to the respective CRSF energy via $C_{\text{CRSF},\sigma}$.

(^c) Coupled to F_{PL} via $F_{10\text{keV}}/F_{\text{PL}}$.

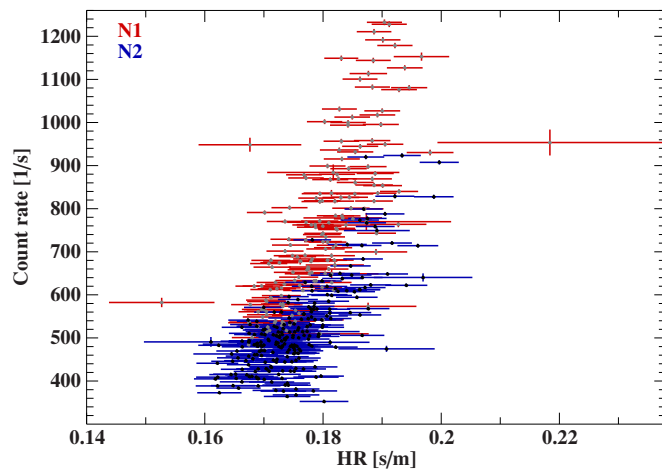


(a) N1

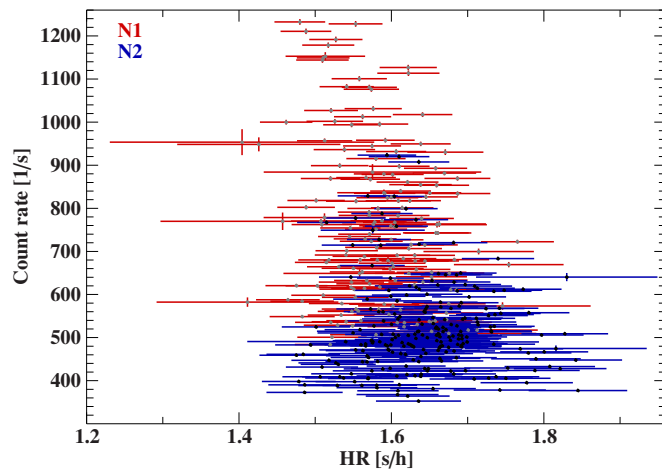


(b) N2

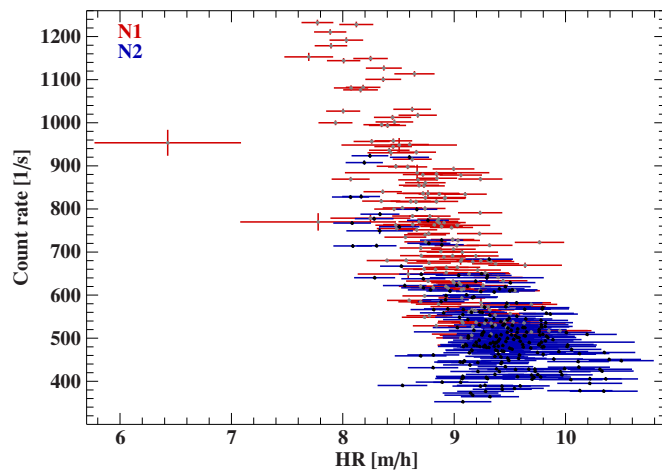
Figure 6.4: The plots show the best fit of the flux-averaged *NuSTAR* observation of N1 (a) and N2 (b) and the respective residuals. Data taken with FPMA is shown in red and FPMB in blue.



(a) s/m



(b) s/h



(c) m/h

Figure 6.5: Hardness-intensity plots of different energy bands of both *NuSTAR* observations of 4U 0115+63. Data from observation N1 is plotted using gray dots and red error bars, while information from N2 is shown black with blue error bars. In both cases the soft band ranges from 3.5 to 5 keV, the medium band from 5 to 15 keV and the hard band from 15 to 50 keV.

In accordance with these findings the HR, using the m and the h band, becomes smaller for increasing count rates, as shown in Figure 6.5 (c).

This behavior hints at a change of the spectrum in the medium energy band, that ranges from 5 to 15 keV, with varying intensity. This change can only result from a spectral component that is located in this energy range. When comparing this to the best-fit parameters listed in Table 6.1 and Table 6.2 it can be seen that both the fundamental CRSF and the “10 keV feature” are located in this energy range. In addition the HRs changed continuously with varying count rate, this could hint towards an intensity dependency of the spectral change.

6.3 Flux-resolved spectroscopy

To further examine this intensity dependency of the spectrum, this section focuses on the analysis of the observed *NuSTAR* spectra at different intensity states.

6.3.1 Selected Off-peak / Peak states

As discussed in Berger (2019) the first approach was to select the start and end times of the peak and off-peak states of the QPOs and use these time intervals to extract partial spectra. Due to the lack of a distinct periodicity, see Berger (2019), the changing shapes of the peaks and the gaps in the light curve, that are a consequence of the satellites orbit, these time intervals had to be selected manually. The light curves of N1 and N2 are shown in Figure 6.6. The selected peak times are plotted in orange, while the off-peak times are highlighted in blue. The gray data points could not be assigned explicitly and were left out.

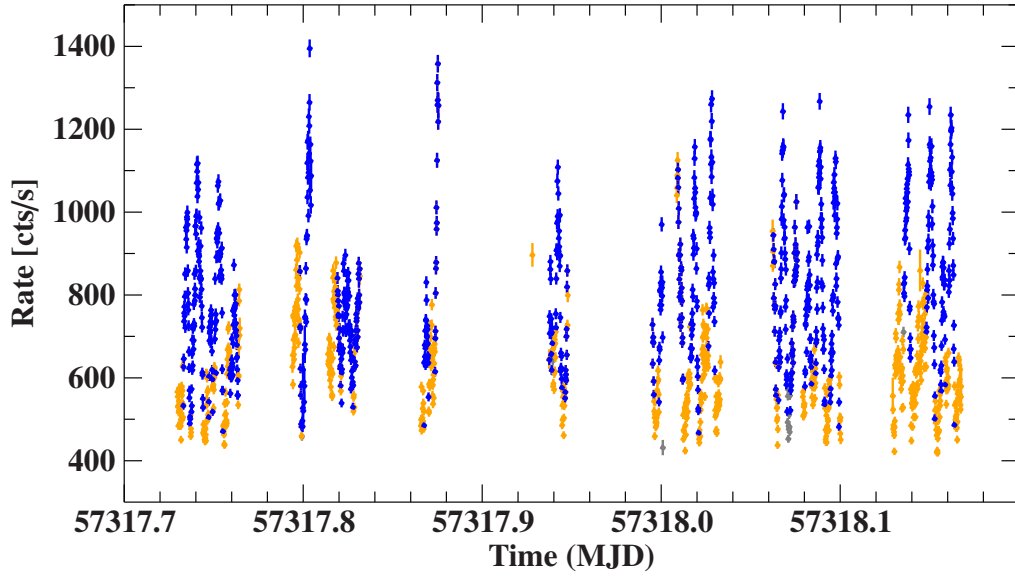
After extracting the peak and off-peak spectra the best-fit parameters of the respective total observation were evaluated. The only modification that was applied was a re-normalization of the parameters to account for the change in the overall flux. The spectra for N1 are shown in Figure 6.7 and in Figure 6.8 for N2.

It can be seen that, even for the slightly more complex model, the same results as in Berger (2019) are obtained. The previous best-fit parameters no longer provides a good description of the spectra around 10 keV. In this energy region the fundamental CRSF and the “10 keV feature” are located. However the energy ranges below ~ 7 keV and above ~ 20 keV are still well described by the previous best fit. This shows that the energies, at which the harmonic CRSFs are located, are not affected by the spectral change. This makes it more likely that the observed variation is caused by the “10 keV feature” that is limited to the affected energy range.

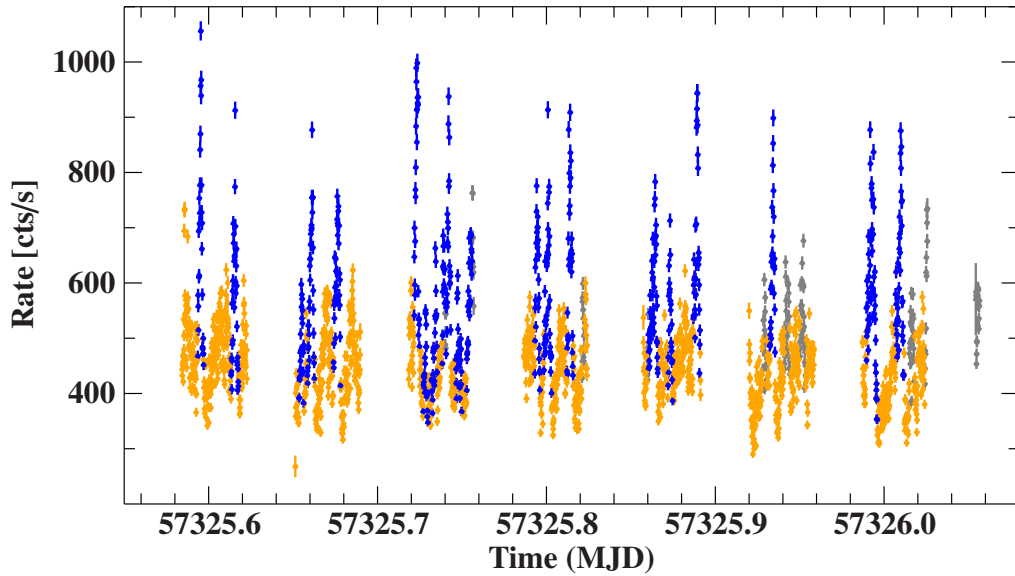
Since the selection of the time intervals was done manually the reproducibility of the results is not optimal. To account for this another approach to split up the observations was tested.

6.3.2 Time-resolved spectroscopy

As a second approach the light curve was partitioned using the only the peak times of the QPOs. An example selection is shown in Figure 6.9 (a). In this way the selection becomes less arbitrary and therefore more reproducible. The time between two consecutive peaks was then split up into ten equally spaced intervals. If the space between two peaks included one



(a) N1

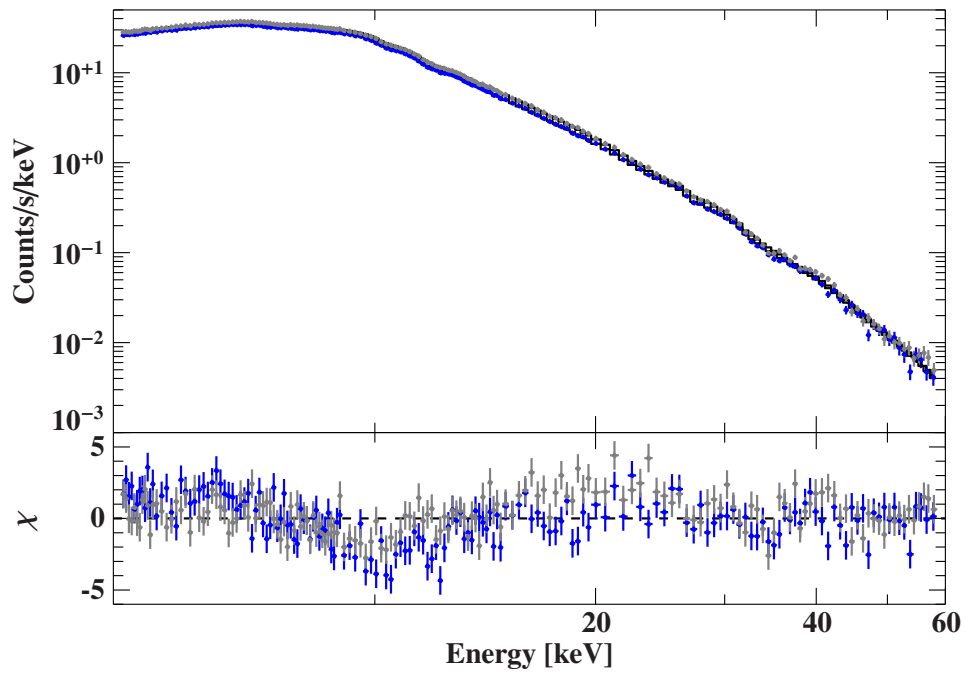


(b) N2

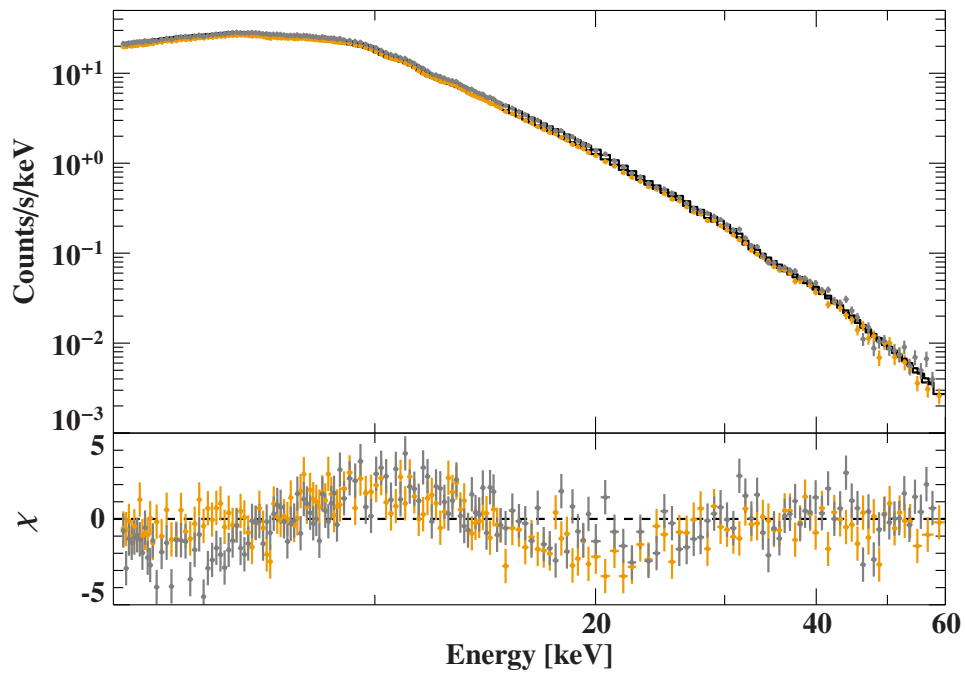
Figure 6.6: Light curves of the combined FPMA and FPMB data of N1 (a) and N2 (b), binned at three times the spin period of the NS. The different colors highlight the fractions that were selected as the peak (blue) and off-peak (orange) states and later used to extract flux-resolved spectra. The gray data points were assigned to neither the peak nor the off-peak state.

of the *NuSTAR* orbit gaps, the data points were rejected. The resulting selection is shown in Figure 6.9 (b), using one part of the light curve of N2 as an example.

The bands, ranging from 0 (blue) to 9 (green) for each interval between two peaks, were then combined to create selection criteria for spectra of the peaks and the intermediate times. In case of the peaks the bands 0, 1, 8 and 9 were combined. For the intermediate times the bands 3, 4, 5 and 6 were selected. The bands 2 and 7 were left out because they could not explicitly be assigned to one of the states. The respective extracted spectra of N1 are shown in Figure 6.10.

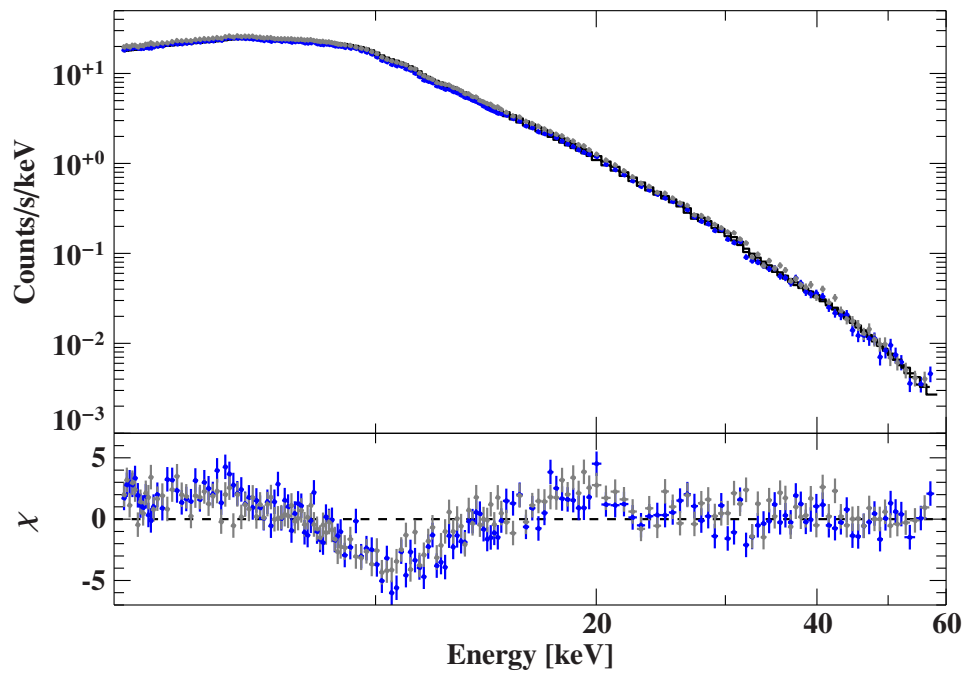


(a) N1: peak

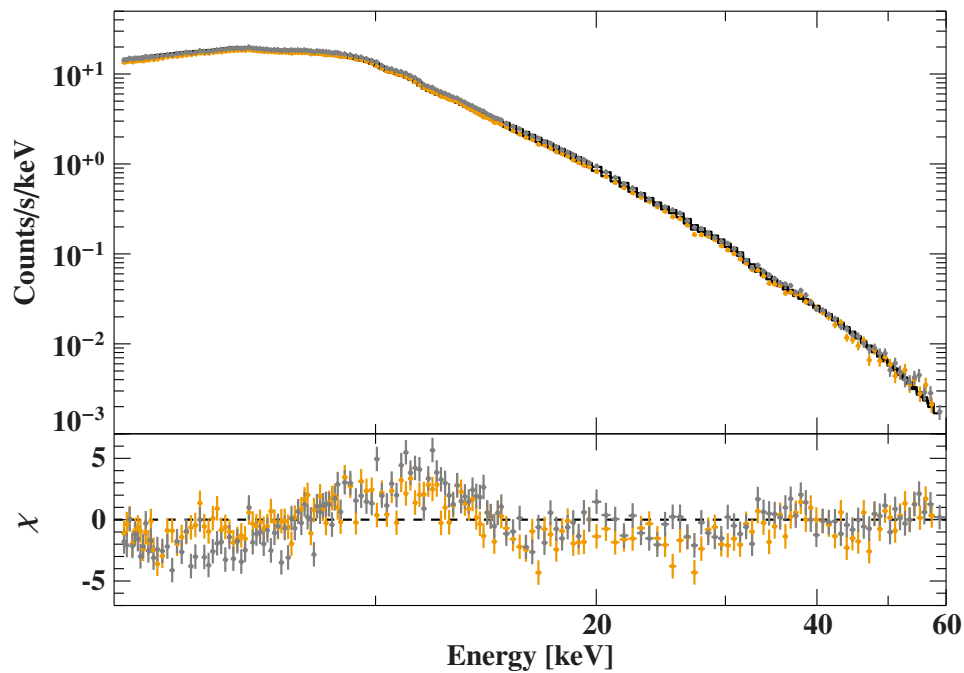


(b) N1: off-peak

Figure 6.7: Spectra of the (a) peak and (b) off-peak states of the *NuSTAR* light curve of N1. The parameters used for the fit function were determined using the total observation and show a deficiency and excess at ~ 11 keV for the peak and off-peak spectra respectively.

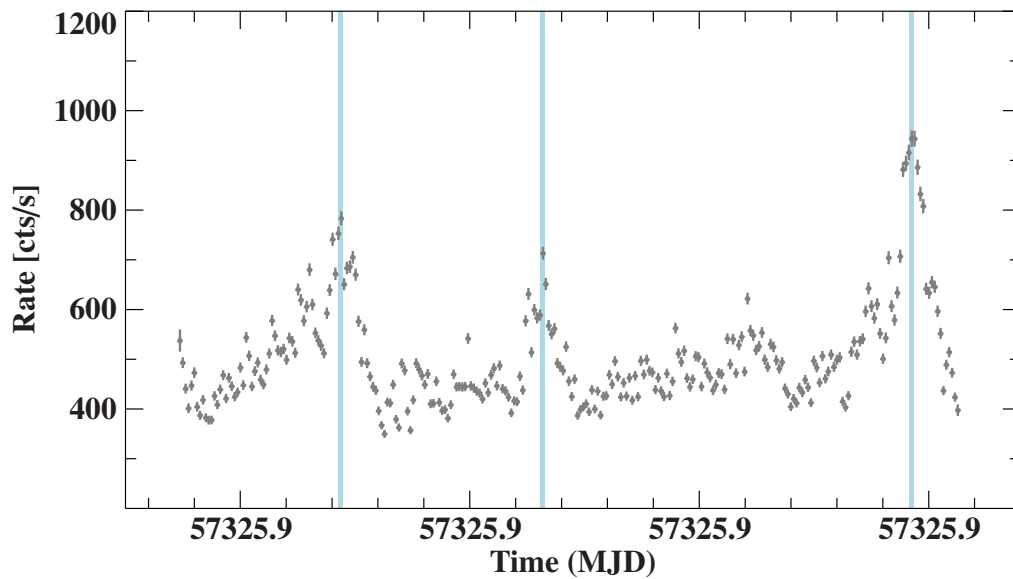


(a) N2: peak

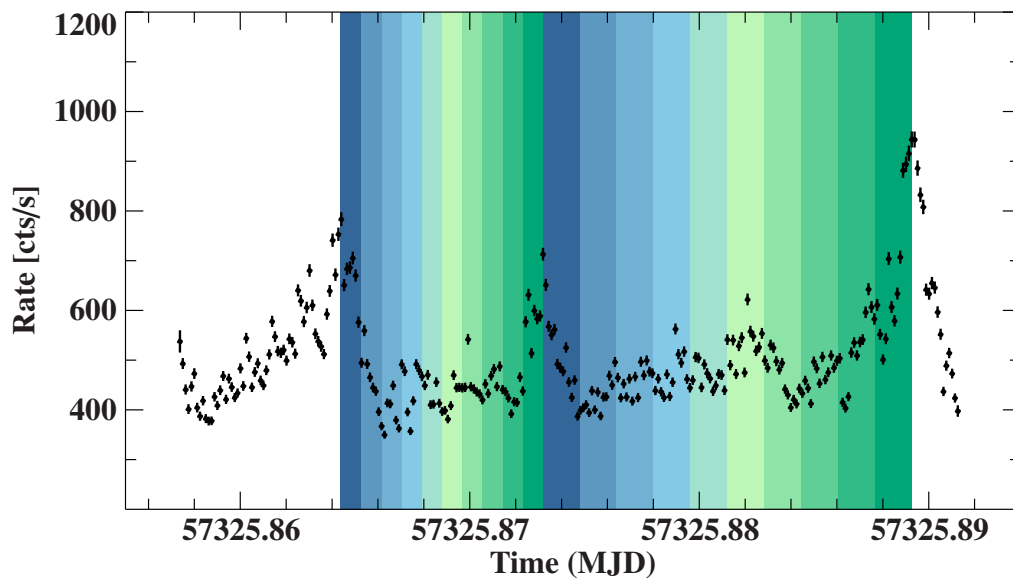


(b) N2: off-peak

Figure 6.8: Spectra of the (a) peak and (b) off-peak states of the *NuSTAR* light curve of N2, following the selection shown in Figure 6.6 (b). The parameters used for the fit function were determined using the total observation and show an deficiency/excess in the residuals around 11 keV.



(a)



(b)

Figure 6.9: The plots shows one of the observed blocks of the light curve of N2. The light curve was rebinned to three times the spin period of the NS. (a): The determined peak times of the observed QPOs are marked using blue vertical lines. (b): This plot visualizes the partition of the light curve in between two consecutive peaks into ten equally spaced parts. The data point prior to the first peak and after the last peak of this segment were not included in the selection.

The spectra of N2 are illustrated in Figure 6.11. The residuals were determined by evaluating and re-normalizing the best-fit parameters of the total *NuSTAR* observations. These parameters are listed in Table 6.2.

To fully utilize this selection, the previously selected peak state, i.e., containing the bands 0, 1, 8 and 9, were further sub-divided into the increasing (band 8 and 9) and the decreasing (band 0 and 1) flanks of the peaks. Figure 6.12 and Figure 6.13 show the spectra and the associated residuals for (a) the increasing and (b) the decreasing parts of the QPO peaks.

The disadvantage of this selection criteria is the large amount of data points that were rejected, due to the gaps in the observed light curves. This also shows in the displayed residuals. It can again be seen that the previous best-fit parameters fail to describe the partial spectra around 10 keV, but the deviation is not as prominent as before. Therefore a method to split up the observations is needed that does not neglect any data, but that can also be easily reproduced.

6.3.3 Selected rates

Since the previous results seem to hint towards an intensity dependency of the spectrum and no specific correlation with the peaks of the light curve, another sectioning of the observation was performed. This time the observed data was grouped into different bands according to the count rate of the data point in the light curve. An advantage of this partition is that no data point had to be rejected. The selected boundaries for the different rate bands are shown in Figure 6.14 (a) for N1 and (b) for N2. These partitions were again used to extract spectra.

To better distinguish the different selected spectra they were named R_{ij} . Here i represents the number of the *NuSTAR* observation, so $i = 1$ in case of N1 and $i = 2$ for N2. The index j ranges from 1 to 4 and consecutively numbers the bands, starting with $j = 1$ for the respective lowest rate, up to $j = 4$ for the bands with the highest rates.

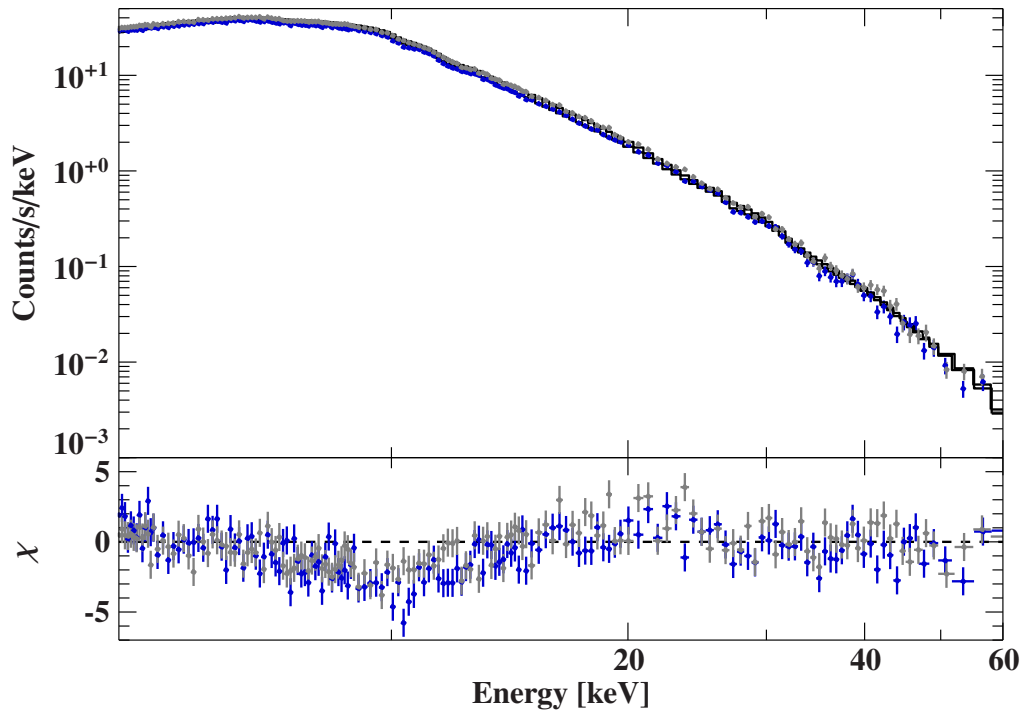
The ranges for the rates were chosen such that the fraction of the total exposure time of the comparable bands, e.g. R11 and R21, are similar. Additionally each partial extraction still had to contain enough information to perform a spectral fit without introducing new constraints to the fit function.

The spectral fit was initialized by evaluating and re-normalizing the best-fit parameters of the corresponding total *NuSTAR* observation, as listed in Table 6.2. The resulting residuals are shown in Figure 6.15 (a) for R11 to R14 and (b) for R21 to R24.

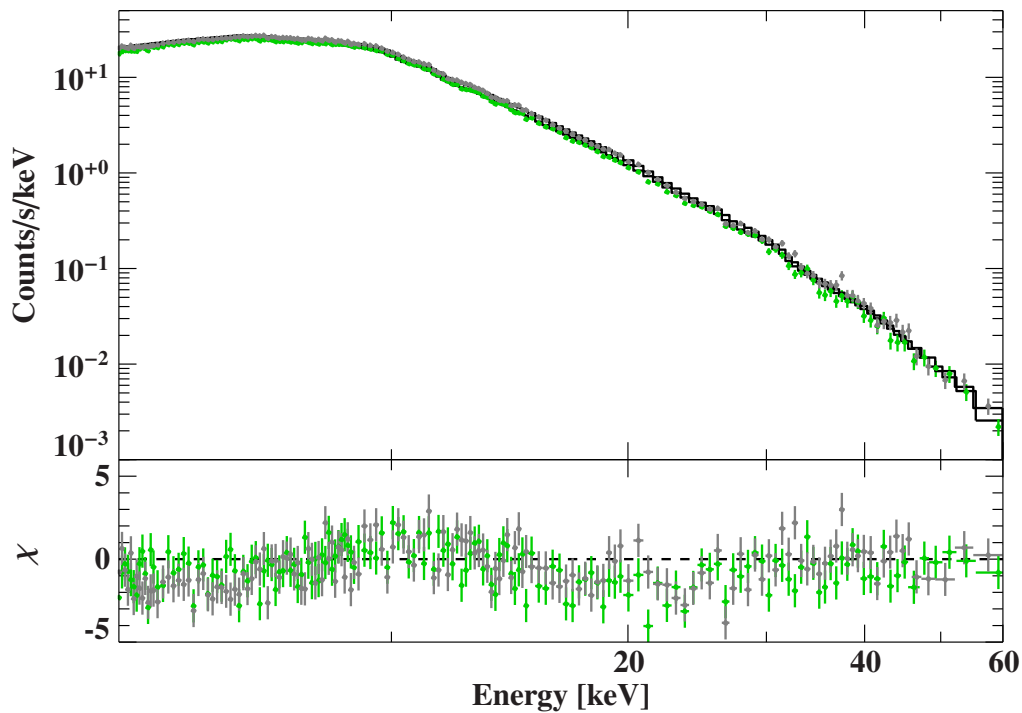
Similar to the residuals shown in the previous sections, the parameters describing the averaged observations do not fit the individual spectra. Again the fit shows a deviation from the spectra around 10 keV. However using this more detailed partition of the data points, the transition in the residuals, from an excess at the lowest count rate to the deficit at the highest count rate, can be observed.

The parameters describing the flux-resolved spectra were determined by re-fitting the previous parameters. The resulting parameter sets for the partial observations of N1 and N2 are listed in Table 6.3 and in Table 6.4 respectively. The plotted residuals for all eight selected spectra are shown in Figure 6.16.

To better visualize the part of the fit that describes the “10 keV feature”, the ratio was plotted after removing the contribution of this component. The results are shown in Figure 6.17.

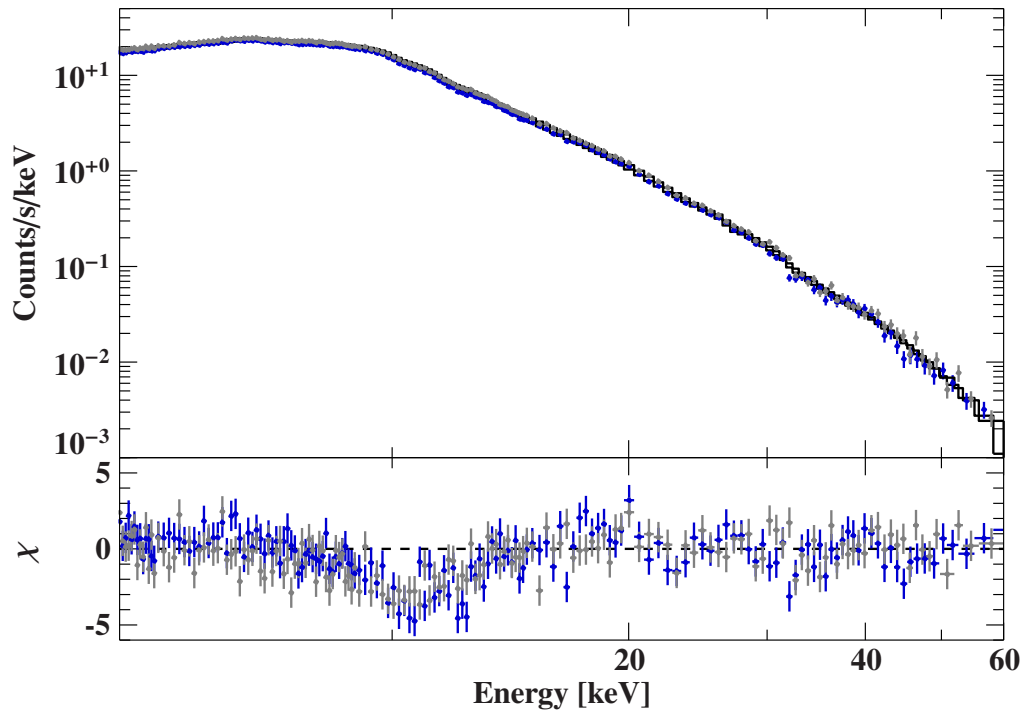


(a) N1: peak

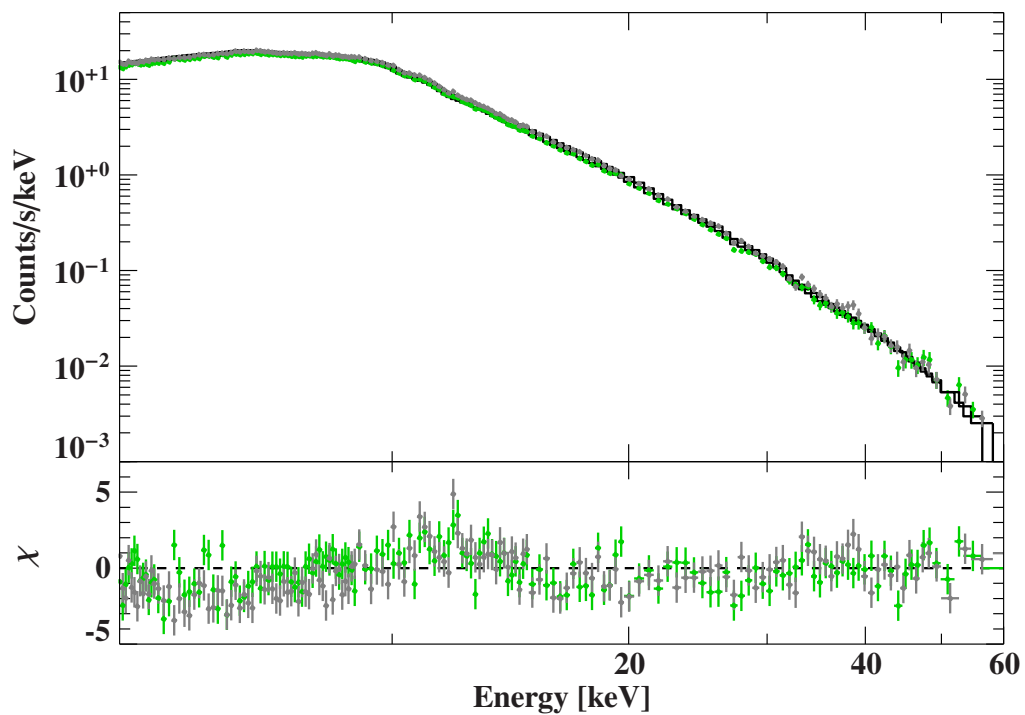


(b) N1: off-peak

Figure 6.10: Spectra of the (a) peak and (b) off-peak states of the *NuSTAR* light curve of N1 (FPMA: gray, FPMB: blue/green). The spectra were extracted using the first and last two segments each of the time selection.

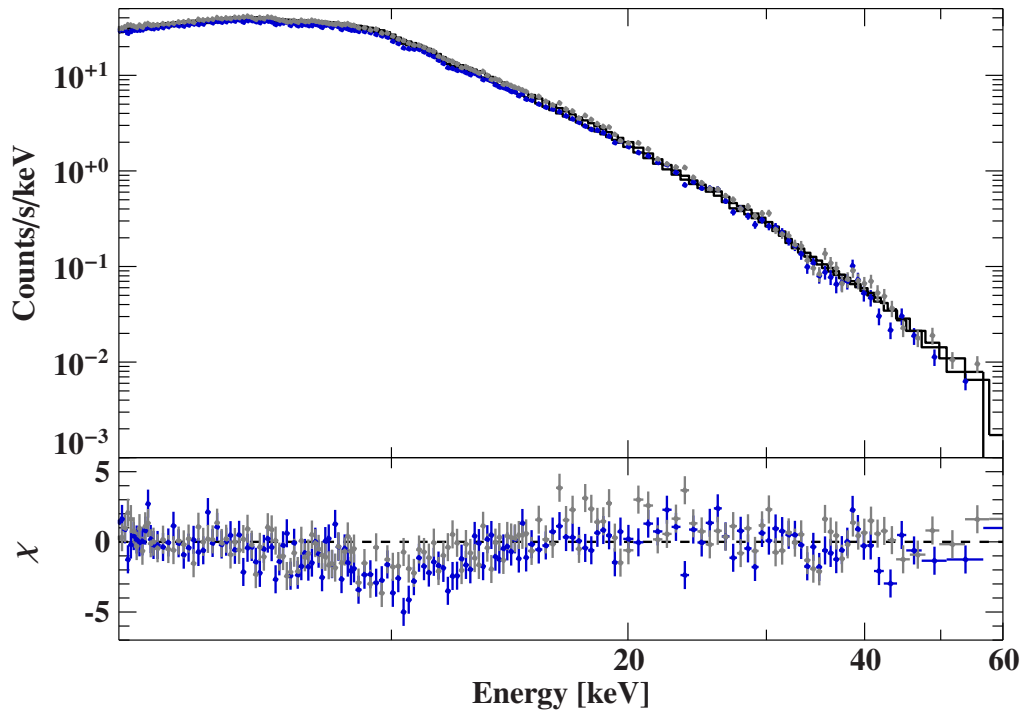


(a) N2: peak

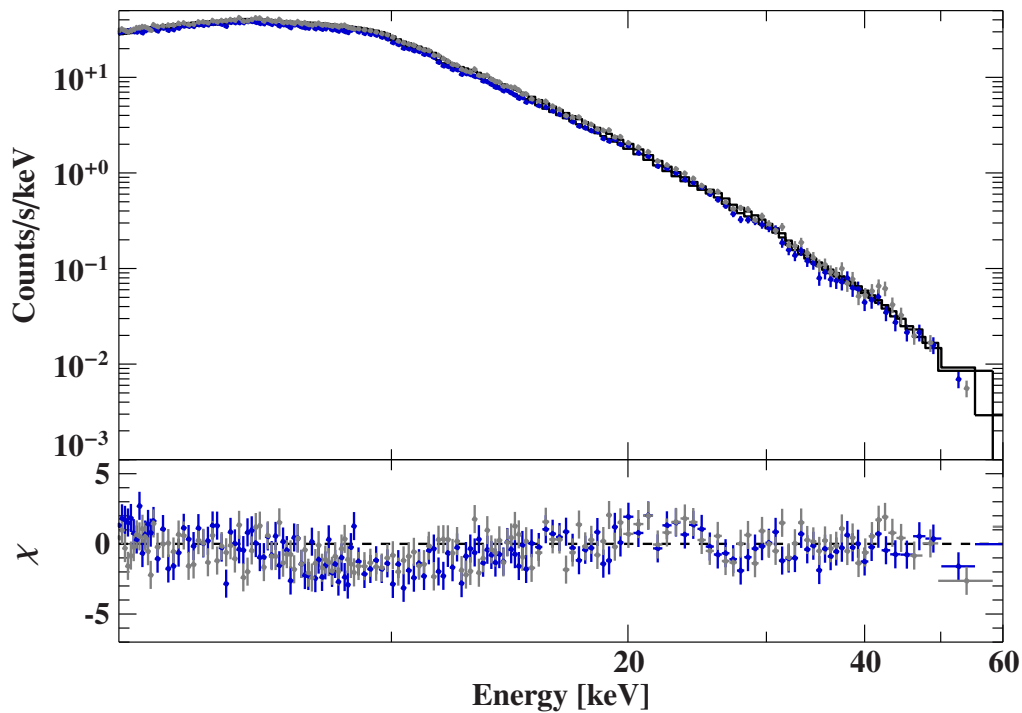


(b) N2: off-peak

Figure 6.11: Spectra of the (a) peak and (b) off-peak states of the *NuSTAR* light curve of N2 (FPMA in gray and FPMB in blue/green). For the extraction the segments 4 to 7, of the selection shown in Figure 6.9 (b), were used.

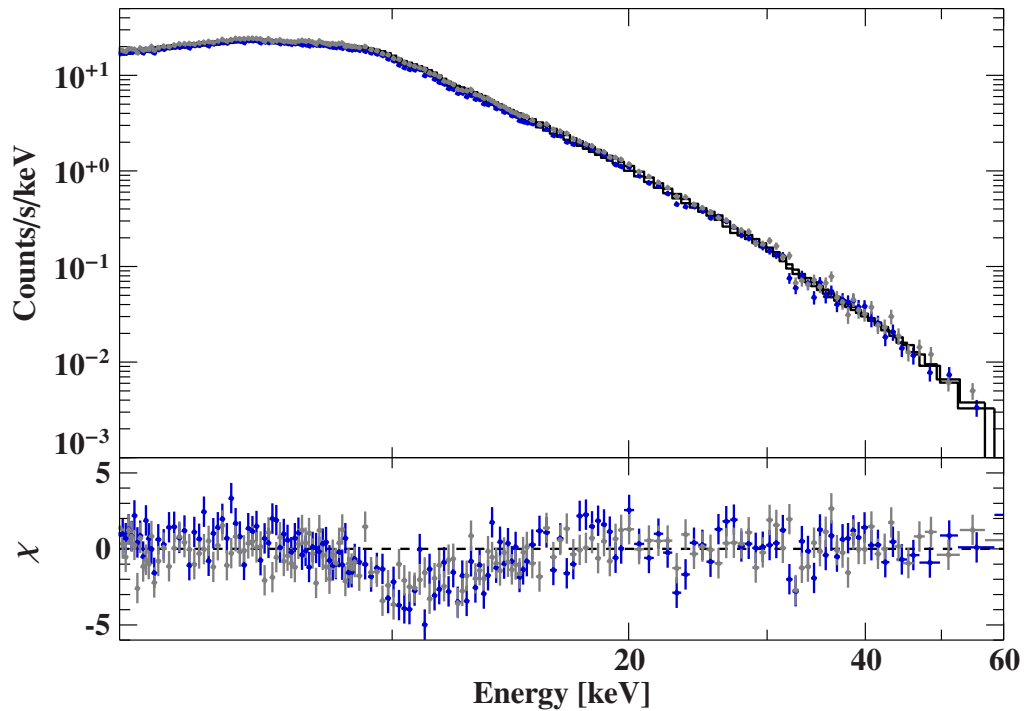


(a) N1: increasing flanks of the peaks

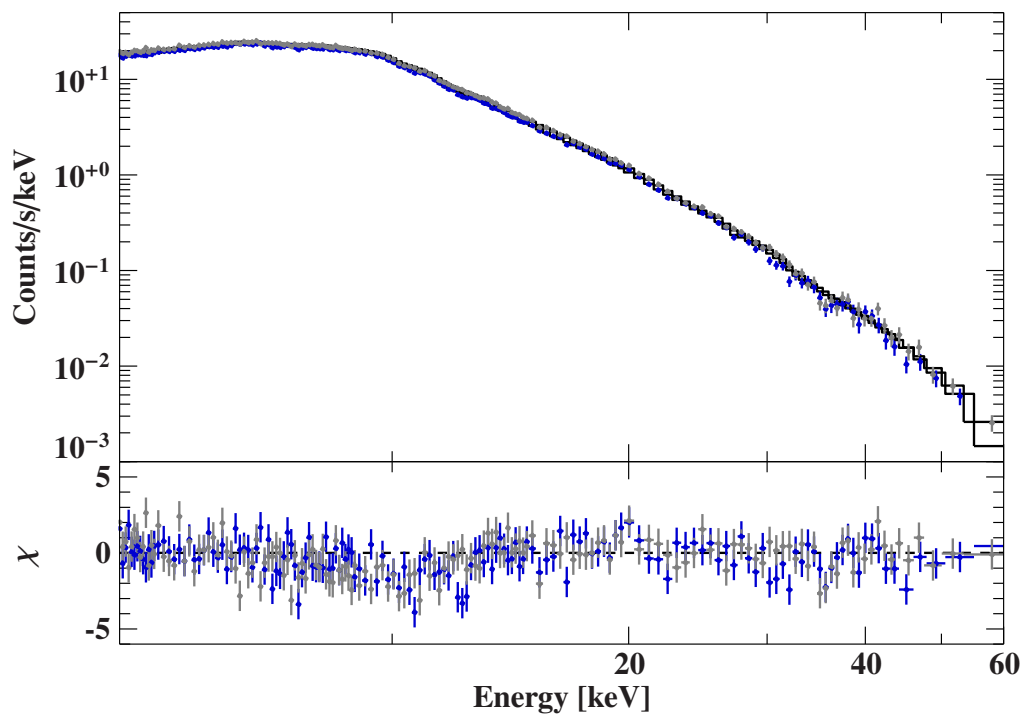


(b) N1: decreasing flanks of the peaks

Figure 6.12: Spectra of the (a) increasing and (b) decreasing parts of the peak states of the *NuSTAR* light curve of N1 (FPMA: gray, FPMB: blue). The spectra for (a) were extracted using the time bands 0 and 1, the spectra for (b) used the time bands 8 and 9 for the extraction.

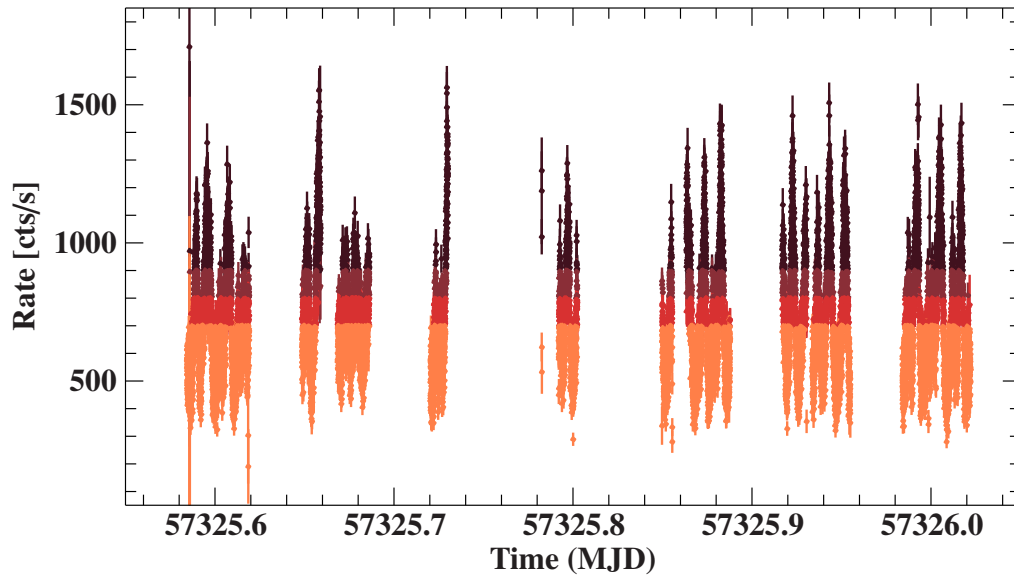


(a) N2: increasing flanks of the peaks

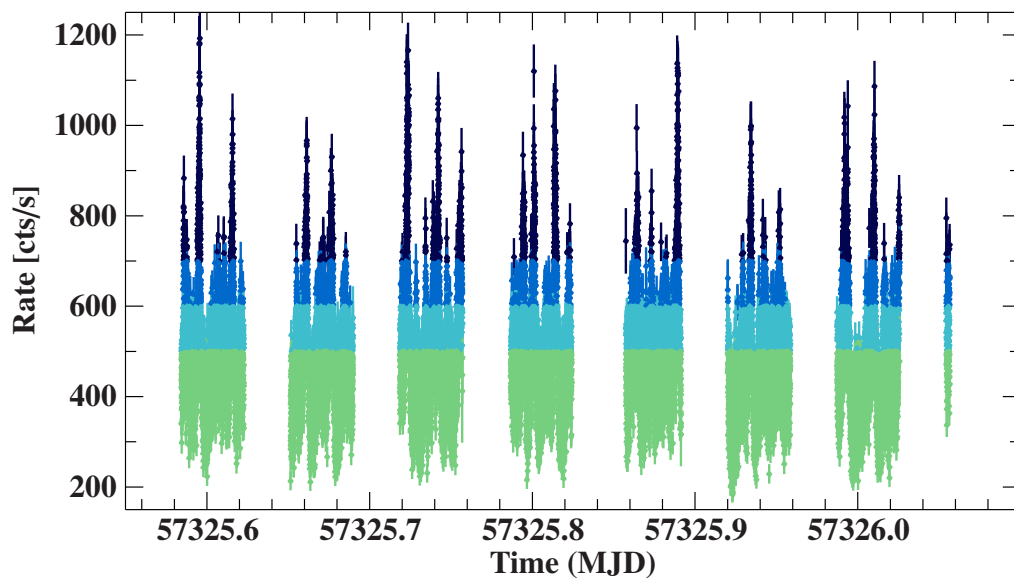


(b) N2: decreasing flanks of the peaks

Figure 6.13: Spectra of the (a) increasing and (b) decreasing flanks of the peak states of the *NuSTAR* light curve of N2 (FPMA in gray and FPMB in blue). For the extraction (a) the segments 0 and 1, for (b) the segments 8 and 9 of the selection shown in Figure 6.9 (b), were used.

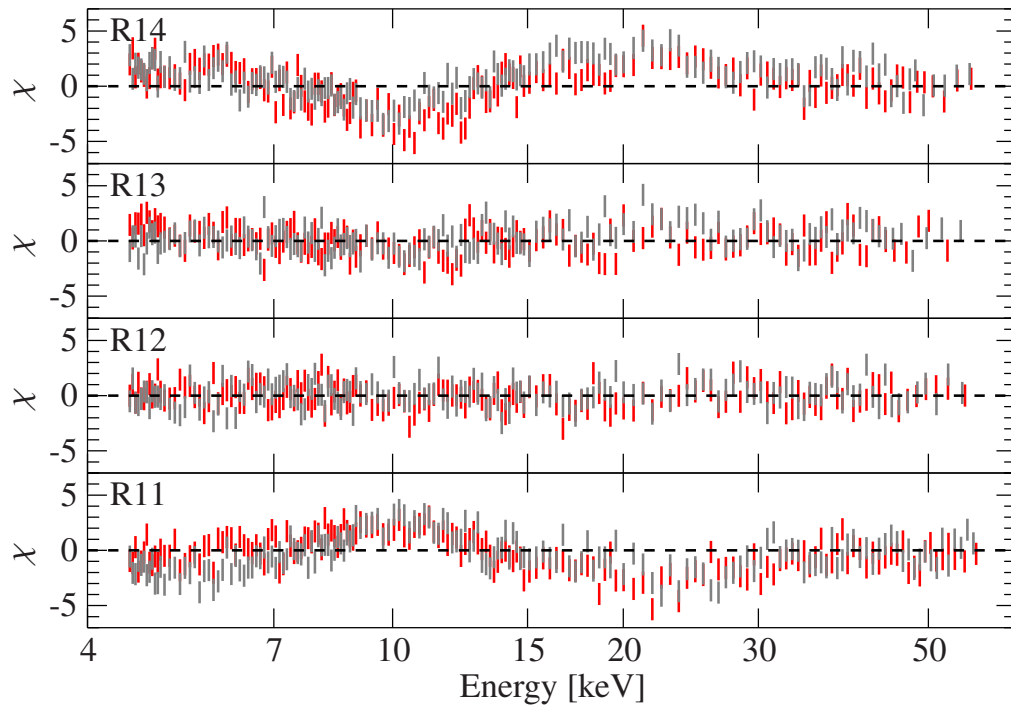


(a) N1

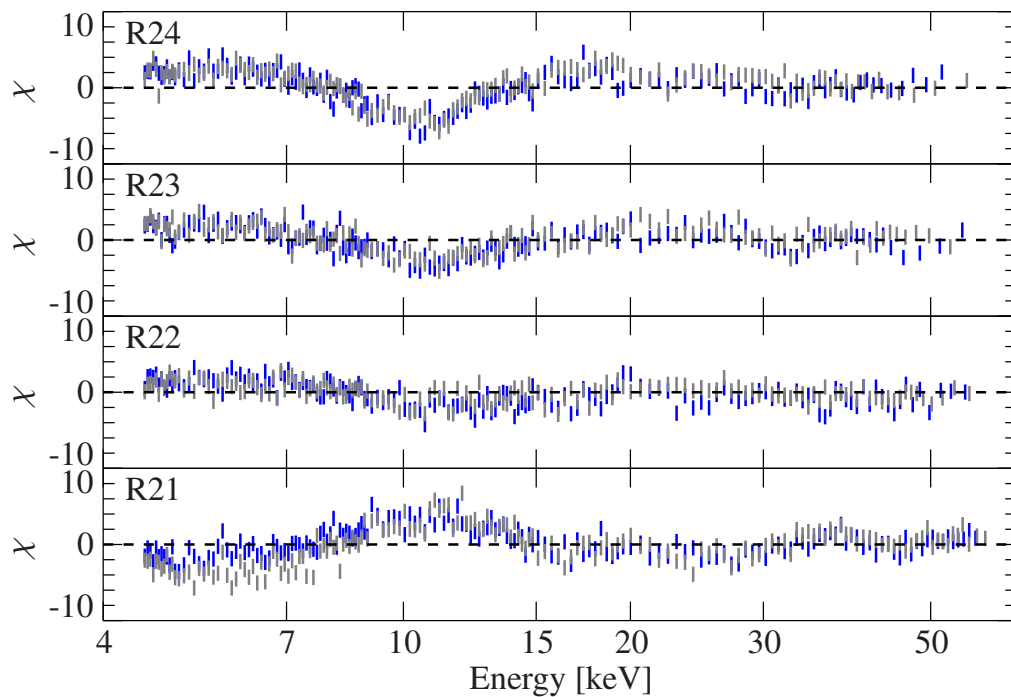


(b) N2

Figure 6.14: Light curves of the combined FPMA and FPMB data, using 1 s binning. The different shaded colors, red in case of N1 and blue for N2, illustrate the selection of the observations into four comparable rate bands.



(a) N1



(b) N2

Figure 6.15: Residuals of the flux-resolved spectra using the best-fit parameters obtained by fitting the corresponding flux-averaged spectra.

Table 6.3: Best parameters of the spectral fit of the fluxresolved *NuSTAR* observations of N1 with confidence limits.

Parameter	Unit	R11	R12	R13	R14
c_{FPMA}		1.00 [†]	1.00 [†]	1.00 [†]	1.00 [†]
c_{FPMB}		0.9659 ± 0.0024	0.959 ± 0.004	0.960 ± 0.005	0.953 ± 0.004
N_{H}	$\times 10^{22} \text{ cm}^{-2}$	3.2 ± 1.1	< 2.15	< 2.81	$2.7^{+1.8}_{-1.6}$
$E_{\text{CRSF},0}$	keV	11.80 ± 0.13	$11.60^{+0.19}_{-0.18}$	$11.79^{+0.17}_{-0.16}$	$11.80^{+0.18}_{-0.21}$
$\sigma_{\text{CRSF},0}$	keV	1.32 ^b	1.14 ^b	0.911 ^b	1.24 ^b
$D_{\text{CRSF},0}$		$0.18^{+0.05}_{-0.04}$	$0.13^{+0.06}_{-0.05}$	$0.15^{+0.07}_{-0.05}$	$0.21^{+0.08}_{-0.06}$
$E_{\text{CRSF},1}$	keV	23.6 ^a	23.2 ^a	23.6 ^a	23.6 ^a
$\sigma_{\text{CRSF},1}$	keV	2.64 ^b	2.28 ^b	1.82 ^b	2.47 ^b
$D_{\text{CRSF},1}$		$1.42^{+0.28}_{-0.24}$	$0.97^{+0.34}_{-0.28}$	$0.43^{+0.27}_{-0.19}$	$0.72^{+0.29}_{-0.23}$
$E_{\text{CRSF},2}$	keV	35.4 ^a	34.8 ^a	35.4 ^a	35.4 ^a
$\sigma_{\text{CRSF},2}$	keV	3.97 ^b	3.42 ^b	2.73 ^b	3.71 ^b
$D_{\text{CRSF},2}$		2.0 ± 0.7	$2.4^{+1.0}_{-0.9}$	$1.7^{+1.0}_{-0.7}$	$2.0^{+0.9}_{-0.8}$
$E_{\text{CRSF},3}$	keV	47.2 ^a	46.4 ^a	47.1 ^a	47.2 ^a
$\sigma_{\text{CRSF},3}$	keV	5.29 ^b	4.56 ^b	3.64 ^b	4.95 ^b
$D_{\text{CRSF},3}$		$2.1^{+1.7}_{-1.6}$	$3.5^{+2.3}_{-2.0}$	$1.9^{+2.2}_{-1.7}$	$2.9^{+1.1}_{-1.8}$
Γ		$0.43^{+0.07}_{-0.08}$	$0.29^{+0.17}_{-0.19}$	< 0.420	$0.30^{+0.18}_{-0.27}$
E_{fold}	keV	9.5 ± 0.5	$9.7^{+0.9}_{-0.8}$	$9.2^{+1.0}_{-0.8}$	9.4 ± 0.8
F_{PL}	$\text{keV s}^{-1} \text{ cm}^{-2}$	7.28 ± 0.26	8.8 ± 0.7	9.5 ± 0.9	$13.0^{+1.2}_{-1.3}$
$A_{10\text{keV}}$	$\text{ph s}^{-1} \text{ cm}^{-2}$	1.00 [†]	1.00 [†]	1.00 [†]	1.00 [†]
$E_{10\text{keV}}$	keV	$7.30^{+0.29}_{-0.31}$	$6.3^{+0.7}_{-0.9}$	5.3 ± 1.1	$5.3^{+1.2}_{-1.5}$
$\sigma_{10\text{keV}}$	keV	$3.49^{+0.20}_{-0.19}$	4.0 ± 0.4	4.5 ± 0.5	$4.4^{+0.7}_{-0.6}$
$F_{10\text{keV}}$	$\text{keV s}^{-1} \text{ cm}^{-2}$	2.07 ^c	3.16 ^c	3.95 ^c	4.13 ^c
$A_{\text{FeK}\alpha}$	$\text{ph s}^{-1} \text{ cm}^{-2}$	0.0012 ± 0.0004	0.0018 ± 0.0008	0.0021 ± 0.0011	0.0014 ± 0.0010
$E_{\text{FeK}\alpha}$	keV	6.40 [†]	6.40 [†]	6.40 [†]	6.40 [†]
$A_{\text{FeXXV K}\alpha}$	$\text{ph s}^{-1} \text{ cm}^{-2}$	$(7 \pm 4) \times 10^{-4}$	0.0021 ± 0.0008	< 0.00158	0.0012 ± 0.0010
$E_{\text{FeXXV K}\alpha}$	keV	6.69 [†]	6.69 [†]	6.69 [†]	6.69 [†]
$A_{\text{FeXXVI K}\alpha}$	$\text{ph s}^{-1} \text{ cm}^{-2}$	$(3 \pm 4) \times 10^{-4}$	< 0.000898	< 0.00179	< 0.00169
$E_{\text{FeXXVI K}\alpha}$	keV	6.97 [†]	6.97 [†]	6.97 [†]	6.97 [†]
$F_{10\text{keV}}/F_{\text{PL}}$		0.28 ± 0.04	$0.36^{+0.10}_{-0.07}$	$0.42^{+0.13}_{-0.10}$	$0.32^{+0.13}_{-0.09}$
$c_{\text{CRSF},\sigma}$		$0.112^{+0.012}_{-0.011}$	0.098 ± 0.016	$0.077^{+0.022}_{-0.017}$	$0.105^{+0.018}_{-0.015}$
red. χ^2 / d.o.f.		1.08 / 318	1.06 / 305	1.21 / 300	1.21 / 309

(†) Fixed.

(a) Set to the multiple integer value of $E_{\text{CRSF},0}$.

(b) Coupled to the respective CRSF energy via $c_{\text{CRSF},\sigma}$.

(c) Coupled to F_{PL} via $F_{10\text{keV}}/F_{\text{PL}}$.

Table 6.4: Best parameters of the spectral fit of the fluxresolved *NuSTAR* observations of N2 with confidence limits.

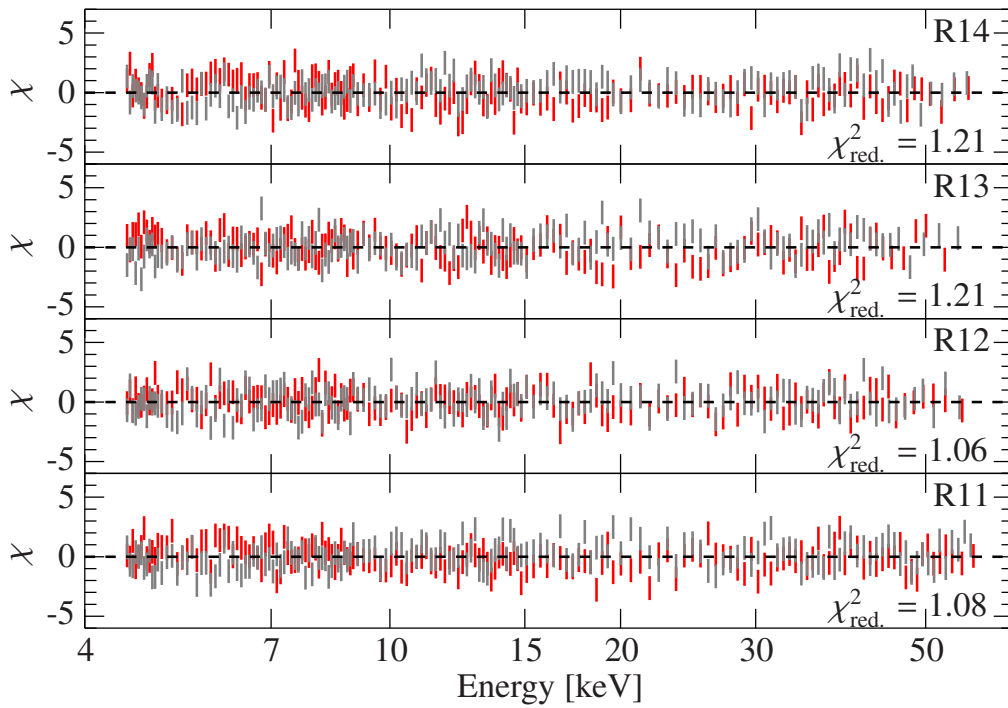
Parameter	Unit	R21	R22	R23	R24
C_{FPMA}		1.00 [†]	1.00 [†]	1.00 [†]	1.00 [†]
C_{FPMB}		0.9823 ± 0.0021	0.972 ± 0.004	0.969 ± 0.005	0.968 ± 0.006
N_{H}	$\times 10^{22} \text{ cm}^{-2}$	1.7 ± 1.0	< 0.903	< 1.91	< 2.90
$E_{\text{CRSF},0}$	keV	12.02 ± 0.22	$11.93^{+0.17}_{-0.16}$	11.40 ± 0.21	$11.27^{+0.19}_{-0.16}$
$\sigma_{\text{CRSF},0}$	keV	1.82 ^b	1.12 ^b	1.03 ^b	1.00 ^b
$D_{\text{CRSF},0}$		$0.17^{+0.18}_{-0.08}$	$0.09^{+0.05}_{-0.04}$	$0.13^{+0.08}_{-0.06}$	$0.16^{+0.08}_{-0.05}$
$E_{\text{CRSF},1}$	keV	24.0 ^a	23.9 ^a	22.8 ^a	22.5 ^a
$\sigma_{\text{CRSF},1}$	keV	3.64 ^b	2.25 ^b	2.06 ^b	2.01 ^b
$D_{\text{CRSF},1}$		$1.8^{+0.7}_{-0.5}$	$0.84^{+0.32}_{-0.24}$	$0.60^{+0.29}_{-0.23}$	$1.00^{+0.56}_{-0.25}$
$E_{\text{CRSF},2}$	keV	36.1 ^a	35.8 ^a	34.2 ^a	33.8 ^a
$\sigma_{\text{CRSF},2}$	keV	5.46 ^b	3.37 ^b	3.09 ^b	3.01 ^b
$D_{\text{CRSF},2}$		$2.6^{+1.1}_{-1.0}$	$2.3^{+1.2}_{-1.0}$	$2.1^{+1.2}_{-0.9}$	$1.8^{+1.9}_{-0.8}$
$E_{\text{CRSF},3}$	keV	48.1 ^a	47.7 ^a	45.6 ^a	45.1 ^a
$\sigma_{\text{CRSF},3}$	keV	7.28 ^b	4.49 ^b	4.12 ^b	4.01 ^b
$D_{\text{CRSF},3}$		< 4.49	$1.9^{+2.5}_{-1.9}$	< 3.39	< 3.30
Γ		0.39 ± 0.07	$0.25^{+0.10}_{-0.09}$	$0.32^{+0.14}_{-0.11}$	< 0.345
E_{fold}	keV	$9.5^{+0.6}_{-0.5}$	$8.8^{+0.7}_{-0.6}$	$8.9^{+0.8}_{-0.6}$	$8.1^{+1.1}_{-0.5}$
F_{PL}	$\text{keV s}^{-1} \text{ cm}^{-2}$	$5.65^{+0.28}_{-0.20}$	5.96 ± 0.17	$7.33^{+0.33}_{-0.26}$	9.1 ± 0.6
$A_{10\text{keV}}$	$\text{ph s}^{-1} \text{ cm}^{-2}$	1.00 [†]	1.00 [†]	1.00 [†]	1.00 [†]
$E_{10\text{keV}}$	keV	$7.77^{+0.22}_{-0.18}$	$6.83^{+0.28}_{-0.32}$	7.1 ± 0.5	$6.3^{+0.7}_{-0.9}$
$\sigma_{10\text{keV}}$	keV	$3.20^{+0.12}_{-0.13}$	$3.51^{+0.18}_{-0.16}$	$3.25^{+0.27}_{-0.26}$	$3.4^{+0.5}_{-0.4}$
$F_{10\text{keV}}$	$\text{keV s}^{-1} \text{ cm}^{-2}$	1.59 ^c	1.88 ^c	1.78 ^c	2.02 ^c
$A_{\text{FeK}\alpha}$	$\text{ph s}^{-1} \text{ cm}^{-2}$	$(9.3 \pm 2.3) \times 10^{-4}$	0.0012 ± 0.0004	$0.0025^{+0.0007}_{-0.0008}$	$0.0020^{+0.0010}_{-0.0011}$
$E_{\text{FeK}\alpha}$	keV	6.40 [†]	6.40 [†]	6.40 [†]	6.40 [†]
$A_{\text{Fe}_{\text{XXV}}\text{K}\alpha}$	$\text{ph s}^{-1} \text{ cm}^{-2}$	$(9.1 \pm 2.3) \times 10^{-4}$	$(8 \pm 4) \times 10^{-4}$	0.0014 ± 0.0007	0.0021 ± 0.0010
$E_{\text{Fe}_{\text{XXV}}\text{K}\alpha}$	keV	6.69 [†]	6.69 [†]	6.69 [†]	6.69 [†]
$A_{\text{Fe}_{\text{XXVI}}\text{K}\alpha}$	$\text{ph s}^{-1} \text{ cm}^{-2}$	< 0.000123	$(7 \pm 4) \times 10^{-4}$	< 0.000826	< 0.00164
$E_{\text{Fe}_{\text{XXVI}}\text{K}\alpha}$	keV	6.97 [†]	6.97 [†]	6.97 [†]	6.97 [†]
$F_{10\text{keV}}/F_{\text{PL}}$		$0.281^{+0.025}_{-0.028}$	$0.315^{+0.036}_{-0.030}$	$0.24^{+0.05}_{-0.04}$	$0.22^{+0.08}_{-0.05}$
$c_{\text{CRSF},\sigma}$		$0.151^{+0.032}_{-0.023}$	0.094 ± 0.017	$0.090^{+0.020}_{-0.021}$	$0.089^{+0.025}_{-0.017}$
red. χ^2 / d.o.f.		1.45 / 322	0.99 / 308	1.06 / 298	0.97 / 295

([†]) Fixed.

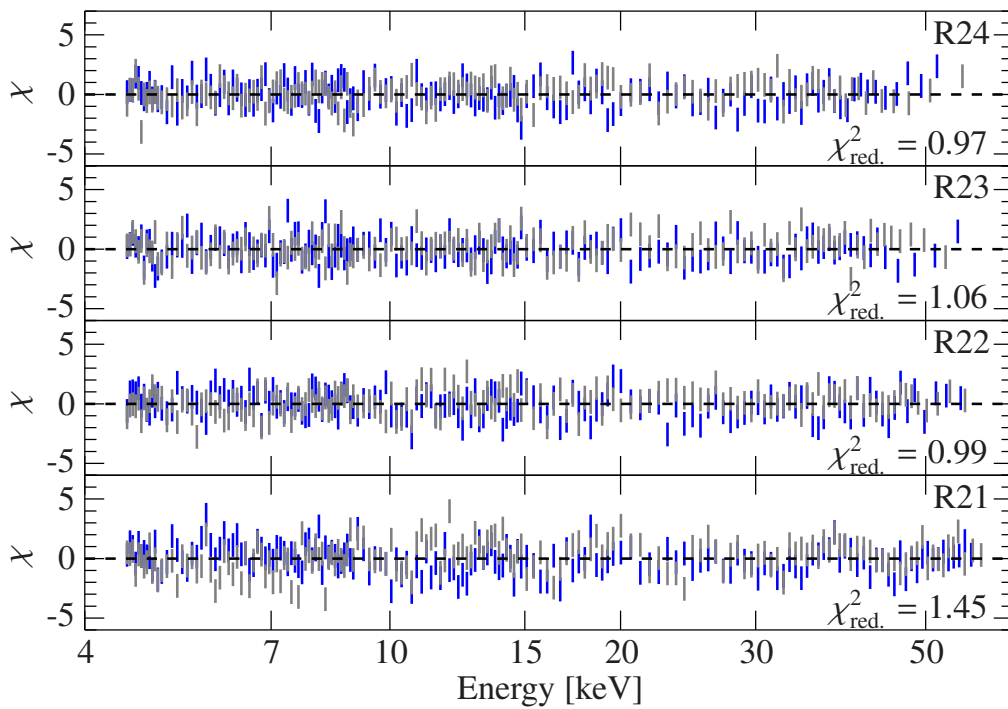
(^a) Set to the multiple integer value of $E_{\text{CRSF},0}$.

(^b) Coupled to the respective CRSF energy via $c_{\text{CRSF},\sigma}$.

(^c) Coupled to F_{PL} via $F_{10\text{keV}}/F_{\text{PL}}$.

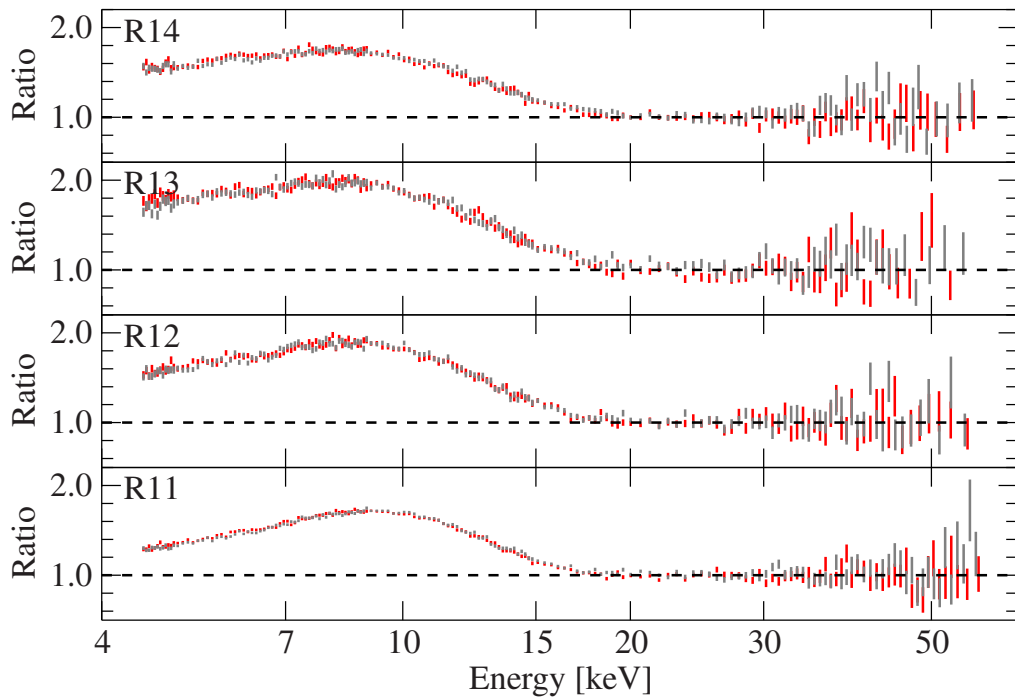


(a) N1

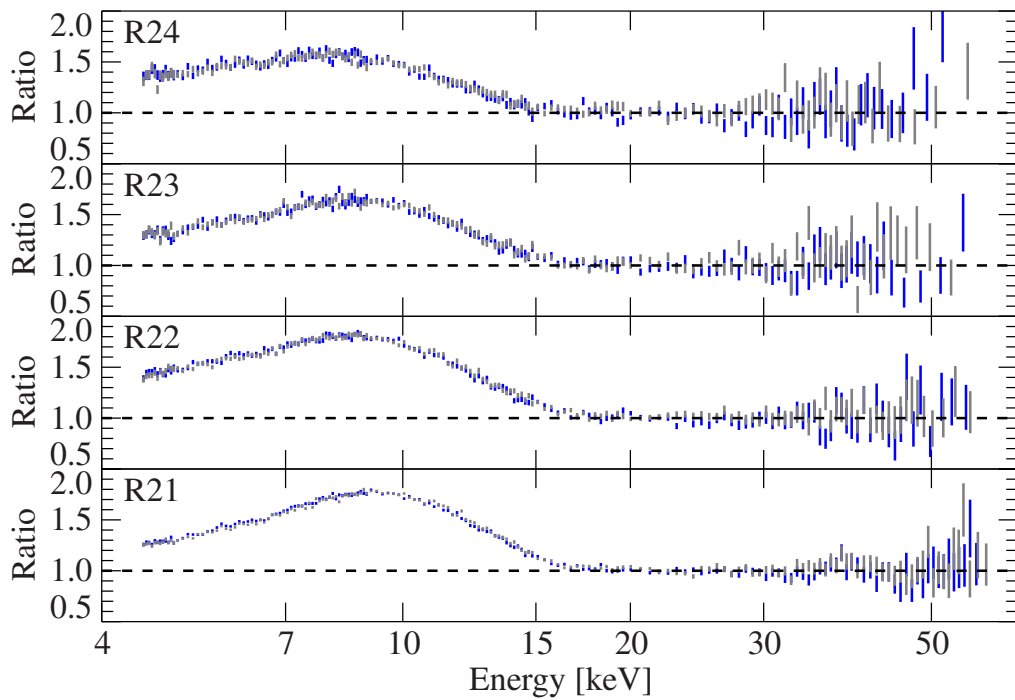


(b) N2

Figure 6.16: Residuals of the individual best fits of the partial spectra. The corresponding parameters of the fits are listed in Table 6.3 in case of N1 and Table 6.4 for N2.



(a) N1



(b) N2

Figure 6.17: Residuals of the spectra of the different rate bands after removing the contribution of the “10 keV feature” from the previous best fit.

6.3.4 2 dimensional confidence contours

While fitting the spectra several difficulties had to be faced, namely the opposing characteristics of the fundamental CRSF and the “10 keV feature”. Additionally the fit algorithm has to be kept from using the fundamental cyclotron line to model the continuum of the spectrum. This lead to a strong correlation between the fit parameters. To examine and visualize these correlations 2 dimensional confidence contours were determined.

A similar approach was used by Müller et al. (2013). In that work they used *RXTE* and *INTEGRAL* observations of the 2008 outburst of 4U 0115+63. In Figure 3, Figure 10 and Figure 11 of Müller et al. (2013) different combinations of parameters were examined. In the first figure they looked at possible correlations of the parameters of the cut-off power-law and the hydrogen abundance. The other two figures focus on the energy of the fundamental cyclotron line, by calculating confidence contours between this energy and several other fit parameters. However for the determination of all of these contours the total observation was used.

For this thesis the calculations were done for the partial spectra that were selected based on the count rate of the respective light curve, see subsection 6.3.3. The 2 dimensional confidence contours were determined to gain additional information on the correlations and to see if they show an intensity dependency.

First the contours of the parameters of the fundamental cyclotron line were calculated. In Figure 6.18 the contours for the energy $E_{\text{CRSF},0}$ and (a) the width $\sigma_{\text{CRSF},0}$ and (b) the depth $D_{\text{CRSF},0}$ are shown. The contours are plotted using shades of red, for observations R11 to R14, and blue, for R21 to R24. Except for R21, only the 3σ contour is given for each observation for clarity. In the case of the contour of R21 the 1, 2 and 3σ contours are given, because of their more complex shape. Due to the constraints that were applied to the parameters of the

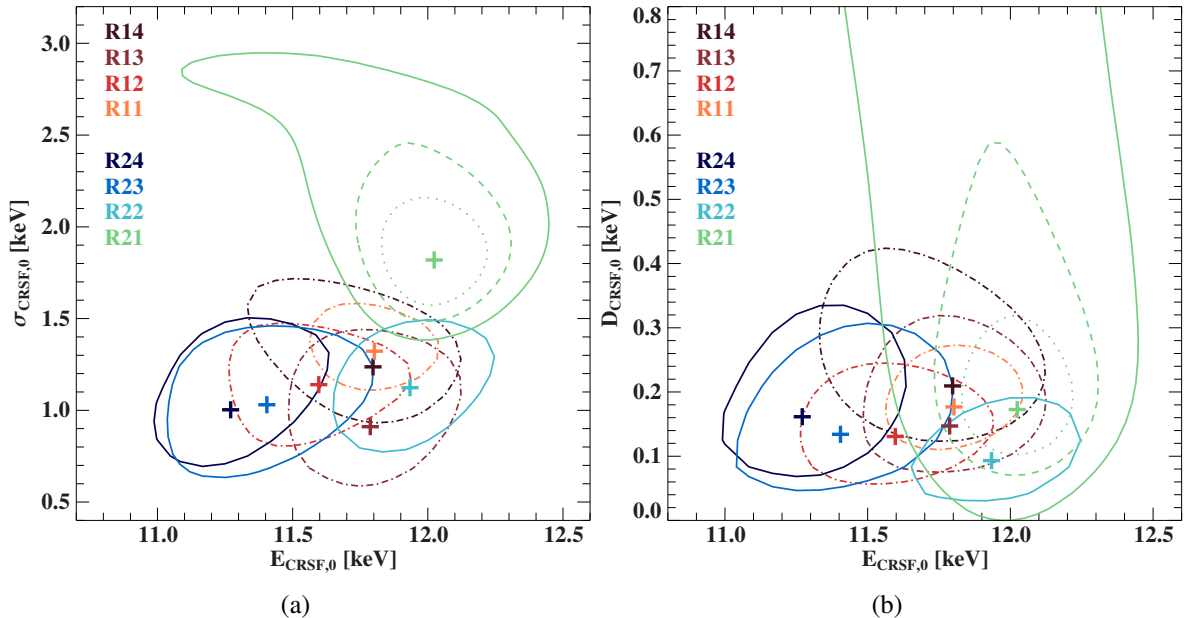


Figure 6.18: 2D contour maps for two sets of parameters of the fundamental CRSF. For the spectra R11 to R14 and R22 to R24 only the 3σ contours are plotted, while for R21 the 1, 2 and 3σ contours are given.

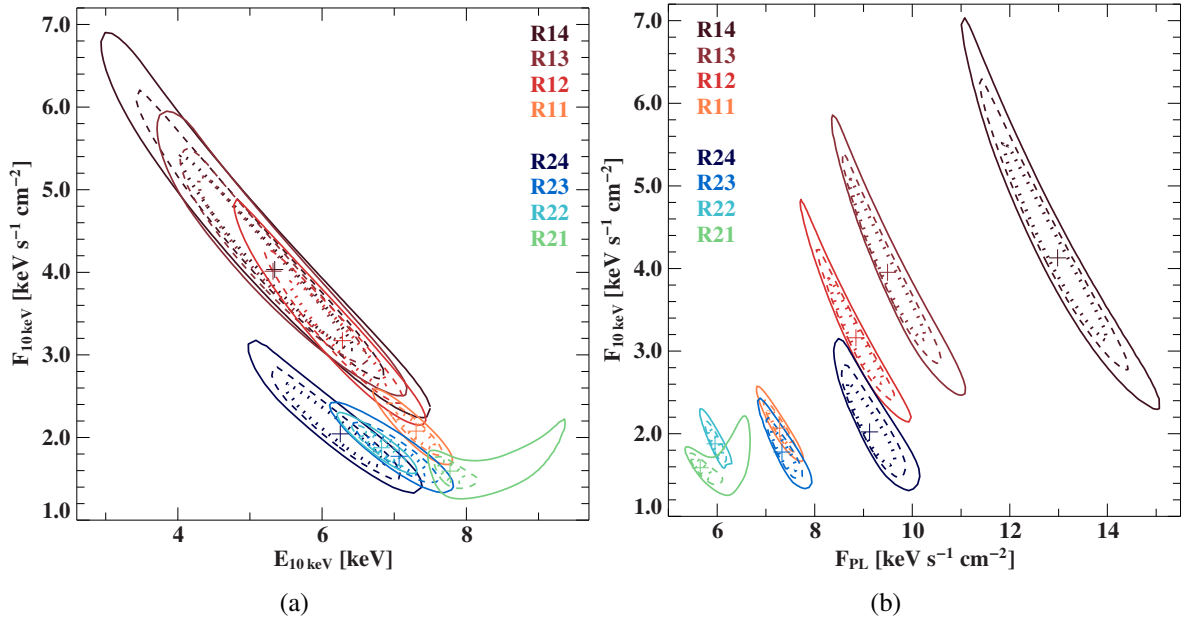


Figure 6.19: Confidence contour maps showing the correlation of the flux of the “10 keV feature” with the energy $E_{10\text{keV}}$ and the flux F_{PL} . For all spectra the 1, 2 and 3 σ contours are plotted using dotted, dashed and solid lines respectively.

CRSFs the fundamental line was used as a representative for all cyclotron lines. For both plots in Figure 6.18 the contours, except for R21, have a nearly circular shape and do overlap. The overlapping of the contours is more prominent in the data from N1, but can still be seen for the spectra from N2 in the overall picture. The shape of the contours does not show any correlation between the parameters of the CRSFs.

Another set of confidence contours was calculated to test for correlations between the flux of the “10 keV feature” and (a) the energy of the “10 keV feature” and (b) the flux of the cut-off power-law that is used to model the continuum. The resulting plots of the 1, 2 and 3 σ contours are shown in Figure 6.19. In both cases the shapes of the determined contours are strongly elongated. Combined with the orientation of the contours, this highlights a strong anti-correlation. It can also be seen that for both observations the contours get bigger with increasing rate. The main difference between the plots shown in Figure 6.19 is the relative positioning of the contours. When considering the energy and the flux of the “10 keV feature” the contours of the respective observations overlap. This shows that the determined anti-correlation is independent of the selected count rate. The small shift between the contours of the different observations might hint towards a dependency of the overall intensity of the observation. On the other hand the contours of the flux of the “10 keV feature” and the cut-off power-law do not overlap. The contours of the different rates of the same observation are shifted perpendicular to the direction of the elongation. This shift confirms a rate dependency of the correlation between the determined fluxes.

Chapter 7

Conclusion and Outlook

In this thesis observations of 4U 0115+63 were studied, focusing on the characteristics of the “10 keV feature”. Therefore a fit describing the averaged spectra was determined. The results were then compared to several partial spectra, that were obtained by sectioning of the light curves of the observations in three different ways. First the visible peaks and the time in between the peaks were selected by hand. For the second partition the times of the peak maxima were determined. The light curve between two consecutive peaks was then separated into ten equally spaced partitions. By combining these sections in different ways the peaks, the increasing and decreasing flank of the peaks and the off-peak states were examined. For the third method divided the observations into different count rate bands.

Comparing the total and the different partial spectra, using the best-fit parameters of the averaged observations, showed a change in the spectral shape around ~ 10 keV. For both *NuSTAR* observations an excess of counts, compared to the averaged data set, was detected for the times in between the peaks and accordingly the low count rates. The associated deficiency could be verified then looking at the peaks of the light curve and at high count rates. The intermediate range showed no variation compared to the respective averaged spectrum.

Further analysing the partial spectra using 2 dimensional confidence contours illustrated a strong anti-correlation of the flux of the “10 keV feature” with the energy of the “10 keV feature” and the flux of the cut-off power-law. Meanwhile no correlation between the parameters of the fundamental CRSF could be verified.

To further continue the analysis the confidence contours of the remaining parameters could be examined to check for any additional correlations. These contours could then also be used to further compare these results, using data from the 2015 outburst, to similar analyses that worked with data from previous outbursts.

Up to now the current results neither allow us to rule out nor to fully confirm one of the possible origins of the “10 keV feature” that were described in section 2.4. To make a conclusive statement about the origin, further results are needed that enable a more detailed physical explanation.

Since in this thesis data of only one source, namely 4U 0115+63, was examined the same analysis could be redone for sources that are also said to contain a “10 keV feature” in their spectra. Studying the behavior of several of these systems could get us closer to being able to explain the origin of this feature or indicate whether or not these additional spectral components

are of the same nature.

As stated before, part of the analysis of this thesis will also be presented in a forthcoming paper. In addition to the already presented work, a more detailed theoretical explanation of the observed behavior is currently under progress and will be discussed in the upcoming publication.

Bibliography

- NuSTAR - Bringing the High Energy Universe into Focus, <https://www.nustar.caltech.edu/> Zugriff am 2022-07-25
- 2018, The Neil Gehrels Swift Observatory, <https://swift.gsfc.nasa.gov/> Zugriff am 2022-07-25
- Alexander S.G., Meszaros P., Bussard R.W., 1989, ApJ 342, 928
- Alpar M.A., Shaham J., 1985, Nat 316, 239
- Arnaud K., Grodon C., Dorman B., 2022, Xspec - An X-Ray Spectral Fitting Package, <https://heasarc.gsfc.nasa.gov/xanadu/xspec/manual/XspecManual.html> Accessed on 2022-09-21
- Ballhausen R., 2021, Ph.D. thesis, Friedrich-Alexander-Universität Erlangen-Nürnberg
- Basko M.M., Sunyaev R.A., 1976, MNRAS 175, 395
- Baykal A., Kızıloğlu Ü., Kızıloğlu N., et al., 2005, A&A 439, 1131
- Becker P.A., Klochkov D., Schönherr G., et al., 2012, A&A 544, A123
- Berger K., 2019, NuSTAR observations of 4U 0115+63
- Bildsten L., 2000, In: Holt S.S., Zhang W.W. (eds.) Cosmic Explosions: Tenth Astrophysics Conference, Vol. 522. American Institute of Physics Conference Series, p.359
- Bissinger né Kühnel M., Kreykenbohm I., Ferrigno C., et al., 2020, A&A 634, A99
- Blay P., 2010, In: Eighth Integral Workshop. The Restless Gamma-ray Universe (INTEGRAL 2010), p. 140
- Boldin P.A., Tsygankov S.S., Lutovinov A.A., 2013, Astronomy Letters 39, 375
- Burrows D.N., Hill J.E., Nousek J.A., et al., 2005, Space Sci. Rev. 120, 165
- Caballero I., Kretschmar P., Santangelo A., et al., 2007, A&A 465, L21
- Capalbi M., Perri M., Saija B., et al., 2005, The SWIFT XRT Data Reduction Guide, https://swift.gsfc.nasa.gov/analysis/xrt_swguide_v1_2.pdf Accessed on 2022-09-26
- Coburn W., Heindl W.A., Rothschild R.E., et al., 2002, ApJ 580, 394

- Ding Y.Z., Wang W., Zhang P., et al., 2021, MNRAS 503, 6045
- Doroshenko V., Tsygankov S.S., Mushtukov A.A., et al., 2017, MNRAS 466, 2143
- Ferrigno C., Becker P.A., Segreto A., et al., 2009, A&A 498, 825
- Finger M.H., Prince T.A., 1997, In: Dermer C.D., Strickman M.S., Kurfess J.D. (eds.) Proceedings of the Fourth Compton Symposium, Vol. 410. American Institute of Physics Conference Series, p.57
- Fürst F., Pottschmidt K., Wilms J., et al., 2014, ApJ 780, 133
- Giacconi R., Murray S., Gursky H., et al., 1972, ApJ 178, 281
- Gornostaev M.I., 2021, MNRAS 501, 564
- Harrison F.A., Craig W.W., Christensen F.E., et al., 2013, ApJ 770, 103
- Heindl W.A., Coburn W., Gruber D.E., et al., 2000, In: McConnell M.L., Ryan J.M. (eds.) The Fifth Compton Symposium, Vol. 510. American Institute of Physics Conference Series, p.173
- Heindl W.A., Coburn W., Gruber D.E., et al., 1999, Astrophys. J., Lett. 521, L49
- Hill J.E., Burrows D.N., Nousek J.A., et al., 2004, In: Flanagan K.A., Siegmund O.H.W. (eds.) X-Ray and Gamma-Ray Instrumentation for Astronomy XIII, Vol. 5165. Society of Photo-Optical Instrumentation Engineers (SPIE) Conference Series, p.217
- Houck J.C., Denicola L.A., 2000, In: Manset N., Veillet C., Crabtree D. (eds.) Astronomical Data Analysis Software and Systems IX, Vol. 216. Astronomical Society of the Pacific Conference Series, p. 591
- Iyer N., Mukherjee D., Dewangan G.C., et al., 2015, MNRAS 454, 741
- Klochkov D., Doroshenko V., Santangelo A., et al., 2012, A&A 542, L28
- Kong L.D., Zhang S., Ji L., et al., 2021, Astrophys. J., Lett. 917, L38
- Kortright J.B., Thompson A.C., 2000, X-Ray Data Booklet - Section 1.2 X-RAY EMISSION ENERGIES, https://xdb.lbl.gov/Section1/Sec_1-2.html Accessed on 2022-09-27
- La Parola V., Cusumano G., Segreto A., D'Ai A., 2016, MNRAS 463, 185
- Liu B.S., Tao L., Zhang S.N., et al., 2020, ApJ 900, 41
- Madsen K.K., Beardmore A., Page K., 2020, X-calibration of NuSTAR and Swift, URL: https://iachec.org/wp-content/presentations/2020/Xcal_swift_nustar.pdf
- Madsen K.K., Burwitz V., Forster K., et al., 2021, arXiv e-prints arXiv:2111.01613
- Makishima K., Mihara T., Ishida M., et al., 1990, Astrophys. J., Lett. 365, L59

- Mihara T., Makishima K., Nagase F., 2004, *ApJ* 610, 390
- Molkov S., Doroshenko V., Lutovinov A., et al., 2021, *Astrophys. J., Lett.* 915, L27
- Motta S.E., Rouco Escorial A., Kuulkers E., et al., 2017, *MNRAS* 468, 2311
- Mueller S., Obst M., Kreykenbohm I., et al., 2010, In: Eighth Integral Workshop. The Restless Gamma-ray Universe (INTEGRAL 2010), p. 116
- Müller S., Ferrigno C., Kühnel M., et al., 2013, *A&A* 551, A6
- Nagel W., 1981, *ApJ* 251, 278
- Nakajima M., Mihara T., Makishima K., Niko H., 2006, *ApJ* 646, 1125
- Negueruela I., Okazaki A.T., 2001, *A&A* 369, 108
- Nelson R.W., Salpeter E.E., Wasserman I., 1993, *ApJ* 418, 874
- Nelson R.W., Wang J.C.L., Salpeter E.E., Wasserman I., 1995, *Astrophys. J., Lett.* 438, L99
- Paul B., Naik S., 2011, *Bulletin of the Astronomical Society of India* 39, 429
- Perri M., Puccetti S., Spagnuolo N., et al., 2021, The NuSTAR Data Analysis Software Guide, https://heasarc.gsfc.nasa.gov/docs/nustar/analysis/nustar_swguide.pdf Accessed on 2022-09-26
- Petre R., Serlemitsos P.J., 1985, *Appl. Opt.* 24, 1833
- Raman G., VarunPaul B., Bhattacharya D., 2021, *MNRAS* 508, 5578
- Rappaport S., Clark G.W., Cominsky L., et al., 1978, *Astrophys. J., Lett.* 224, L1
- Rothschild R.E., Kühnel M., Pottschmidt K., et al., 2017, *MNRAS* 466, 2752
- Soong Y., Swank J.H., 1989, In: Hunt J., Battrick B. (eds.) Two Topics in X-Ray Astronomy, Volume 1: X Ray Binaries. Volume 2: AGN and the X Ray Background, Vol. 1. ESA Special Publication, p. 617
- Staubert R., Shakura N.I., Postnov K., et al., 2007, *A&A* 465, L25
- Staubert R., Trümper J., Kendziorra E., et al., 2019, *A&A* 622, A61
- Suchy S., Pottschmidt K., Wilms J., et al., 2008, *ApJ* 675, 1487
- Tauris T.M., van den Heuvel E.P.J., 2006, Formation and evolution of compact stellar X-ray sources. In: Compact stellar X-ray sources, Vol. 39., p.623
- Thomson B.W., 2014, Ph.D. thesis, University of North Dakota
- Truemper J., Pietsch W., Reppin C., et al., 1978, *Astrophys. J., Lett.* 219, L105
- Unger S.J., Roche P., Negueruela I., et al., 1998, *A&A* 336, 960

- van den Heuvel E.P.J., 2004, In: Schoenfelder V., Lichti G., Winkler C. (eds.) 5th INTEGRAL Workshop on the INTEGRAL Universe, Vol. 552. ESA Special Publication, p. 185
- van der Klis M., Stella L., White N., et al., 1987, ApJ 316, 411
- Vasco D., Staubert R., Klochkov D., et al., 2013, A&A 550, A111
- Verner D.A., Ferland G.J., Korista K.T., Yakovlev D.G., 1996, ApJ 465, 487
- Vybornov V., Doroshenko V., Staubert R., Santangelo A., 2018, A&A 610, A88
- Wilms J., Allen A., McCray R., 2000, ApJ 542, 914
- Zhang L., Blaes O., Jiang Y.F., 2022, MNRAS 515, 4371

Acknowledgements

First I want to thank my supervisor **Prof. Dr. Jörn Wilms** for giving me the possibility to continue working at the Dr. Karl Remeis Sternwarte after I finished my Bachelor's thesis there. I want to thank the **XMAG collaboration** and especially the XRBP working group of the observatory for all the productive discussions that lead to questions that could either be solved or will hopefully be solved in the near future. I want to especially thank **Ralf Ballhausen** for answering all my questions on data analysis and **Katja Pottschmidt** for all the discussions and the feedback on my work. Thanks to **Ekaterina Sokolova-Lapa**, **Aafia Zainab**, **Jakob Stierhof**, **Philipp Thalhammer** and **Nicolas Zalot** for the numerous meetings, online as well as offline, the programming advice and for providing me with support on all types of questions whenever I got stuck. I also want to thank **Amy Joyce** for proofreading and checking the understandability of my explanations.

Thanks to all members of the Remeis observatory that made the observatory feel like a second home and not only a working place. To all the people I shared an office with during my time at the observatory: Thanks for all the fun days at work and the discussions that taught me a lot in addition to the work I did for my thesis. I am counting on you that the tradition of our candy office continues on.

I also want to thank all my friends that continuously supported me emotionally and helped me to clear my head whenever I got stuck. Thanks for always being there and listening to my probably confusing monologues whenever I had problems to get my head around something. Lastly my biggest thanks goes out to my parents. Thank you for always supporting me in all possible ways and thank you for believing in me at all times, even when I started to have doubts.

Without all of you this work would not have been possible. Thank you!

Eigenständigkeitserklärung

Hiermit erkläre ich, dass ich die vorliegende Masterarbeit selbstständig verfasst und keine außer den angegebenen Quellen und Hilfsmitteln verwendet habe.

Datum, Ort

Katrin Berger